BRNO UNIVERSITY OF TECHNOLOGY
VYSOKÉ UČENÍ TECHNICKÉ V BRNĚ

FACULTY OF CHEMISTRY
FAKULTA CHEMICKÁ

INSTITUTE OF PHYSICAL AND APPLIED CHEMISTRY
ÚSTAV FYZIKÁLNÍ A SPOTŘEBNÍ CHEMIE

PREPARATION AND CHARACTERIZATION OF NANODIAMONDS MODIFIED WITH BIOCOMPATIBLE POLYMERS

PŘÍPRAVA A CHARAKTERIZACE NANODIAMANTŮ MODIFIKOVANÝCH BIOKOMPATIBILNÍMI POLYMERY

MASTER'S THESIS
DIPLOMOVÁ PRÁCE

AUTHOR
AUTOR PRÁCE

Bc. Klaudia Kvaková

SUPERVISOR
VEDOUCÍ PRÁCE

Mgr. Petr Cígler PhD.

BRNO 2019

BRNO UNIVERSITY OF TECHNOLOGY
FACULTY OF CHEMISTRY

Master's Thesis Assignment

Number of thesis:	FCH-DIP1276/2018	Academic year: 2018/19
Institute:	Institute of Physical and Applied Chemistry	
Student:	**Bc. Klaudia Kvaková**	
Study programme:	Chemistry for Medical Applications	
Study field:	Chemistry for Medical Applications	
Head of thesis:	**Mgr. Petr Cígler PhD.**	

Title of Master's Thesis:

Preparation and characterization of nanodiamonds modified with biocompatible polymers

Master's Thesis assignment:

The outline of the thesis:

The work will include the following individual tasks:

1) Literature search focused on preparation, surface modification and biomedical applications of nanodiamonds

2) Optimization of preparation and purification of diamond nanoparticles stabilized with biocompatible polymers

3) Stability tests of the nanoparticles in environment simulating physiological conditions

4) Physico-chemical characterization (light scattering, zeta potential, electron microscopy)

Deadline for Master's Thesis delivery: 10. 5. 2019

Master's Thesis is necessary to deliver to a secretary of institute in the number of copies defined by the dean. This assignment is part of Master's Thesis.

Bc. Klaudia Kvaková	Mgr. Petr Cígler PhD.	prof. Ing. Miloslav Pekař, CSc.
Student	Head of thesis	Head of institute

In Brno, 31. 1. 2019

prof. Ing. Martin Weiter, Ph.D.
Dean

Abstract

Nanodiamonds (NDs, 250 nm) were oxidized, separated by size and the polyglycerol layer was polymerized on the ND's surface. The polymerization was achieved by acid catalyzed ring opening multi-branching polymerization of glycidol with the hydroxyl and carboxylic groups formed, during oxidation on the NDs surface. The polyglycerol layer increases the stability and biocompatibility of the NDs. After the coating, a terminal propargyl group was introduced by glycidyl propargyl ether addition. The presence of the alkyne group enables further modification using copper(I)-catalyzed alkyne-azide cycloaddition (CuAAC-click). Employing CuAAC click reaction, a mannose (with azide linker) was attached to the NDs surface. Thus prepared NPs were characterised from the physicochemical point of view. The size distribution was measured by dynamic light scattering (DLS), and it was further confirmed by transmission electron microscopy (TEM). Inertness towards biological conditions was evaluated (stability tests in 1xPBS, 10xPBS and 100 % FBS) and zeta potential was measured. Next, fluorescent nanodiamonds (FNDs, 250 nm) with attached D-mannose were prepared. According to the thermogravimetry results, DLS measurement and TEM images, it was determined, that NDs are covered by thin polyglycerol layer. Presence of glycidol coating was further confirmed by stability tests. Presence of attached D-mannose was supported by Fourier-transform infrared spectroscopy (FTIR). Prepared polyglycerol coated NDs are well suited for *in vitro* and *in vivo* testing. That was proven by their stability in high salt concentration media such as phosphate buffer saline (PBS) and low protein binding properties in fetal bovine serum (FBS).

Keywords

fluorescent nanodiamonds, polyglycerol coating, mannose targeting, sentinel node mapping, CuAAC click

Abstrakt

Nanodiamanty (250 nm) boli podrobené oxidácií, a tiež separované podľa veľkosti. Následne bola na povrch nanodiamantov adsorbovaná rozvetvená vrstva polyglycerolu. Táto vrstva vzniká kyslo katalyzovanou „ring opening“ polymeráciou glycidolu s hydroxylovými a karboxylovými skupinami povrchu nanodiamantov. Vzniknutá polyglycerolová vrstva zvyšuje stabilitu a biokompatibilitu nanodiamantov. Po vytvorení polyglycerolovej vrstvy bol do reakcie pridaný glycidyl propargyl éter, čím došlo k terminácií polymerácie, v dôsledku zavedenia propargylu do reakcie. Prítomná trojná väzba umožňuje nové modifikácie povrchu, napr. prostredníctvom CuAAC reakcie. S využitím CuAAC reakcie je možné na povrch fluorescenčných nanodiamantov pripojiť manózu (so spojkou obsahujúcou azidoskupinu). Pripravené nanočastice boli charakterizované použitím fyzikálno chemických metód. Distribúcia veľkosti častíc bola meraná pomocou dynamického rozptylu svetla (DLS), a taktiež bola potvrdená obrazovou analýzou mikrografov z elektrónového transmisného mikroskopu (TEM). Vyhodnotené bolo aj správanie sa nanodiamantov v biologických podmienkach (stabilitné testy v 1xPBS, 10xPBS a 100 % FBS) a bol meraný aj zeta potenciál. Nakoniec boli pripravené fluorescenčné diamanty (250 nm) s naviazanou manózou. Vzhľadom k výsledkom termogravimetrie, meraniam DLS a pozorovania pomocou TEM môžeme povedať, pripravené nanodiamanty sú pokryté tenkou vrstvou polyglycerolu. Prítomnosť manózy bola zistená na základe FTIR spektier. Nami pripravené fluorescenčné nanodiamanty obalené vrstvou polyglycerolu sú vhodné pre ďalšie testovanie *in vitro* a *in vivo* vďaka ich stabilite v médiách s vysokým obsahom solí ako napr. fosfátový pufor (PBS) a nízkemu viazaniu proteínov vo fetalnom bovinnom sere (FBS).

Kľúčové slová

fluorescenčné nanodiamanty, polyglycidolová vrstva, cielenie manózou, vizualizácia sentinelovej uzliny, CuAAC reakcia

KVAKOVÁ, Klaudia. *Preparation and characterization of nanodiamonds modified with biocompatible polymers*. Brno, 2019. Dostupné také z: https://www.vutbr.cz/studenti/zav-prace/detail/117463. Diplomová práce. Vysoké učení technické v Brně, Fakulta chemická, Ústav fyzikální a spotřební chemie. Vedoucí práce Mgr. Petr Cígler, PhD.

DECLARATION

I declare that the diploma thesis has been worked out by myself and that all the quotations from the used literary sources are accurate and complete. The content of the diploma thesis is the property of the Faculty of Chemistry of Brno University of Technology and all commercial uses are allowed only if approved by both the supervisor and the dean of the Faculty of Chemistry, BUT.

.....

student´s signature

ACKNOWLEDGEMENT

I would like to express my very great appreciation to my supervisor, Petr Cígler, for the opportunity to work in his laboratory and his valuable and constructive suggestions during the planning and development of this research work.

I would like to offer my special thanks to Jiří Schimer, for his everyday support, patience, enthusiasm, motivation, and immense knowledge. I could not have imagined having a better advisor and mentor for my MSc. study.

I would like to express my deep gratitude to Ivana Márová for her support, encouragement and advice during my studies at Brno University of Technology.

I would also like to thank the whole Synthetic Nanochemistry Group, which is very friendly and always willing to help and advise. It was great sharing laboratory with all of you!

Last, but not least I would like to thank my parents Bianka & Petr and my brother Kevin for the support I always get from them during my studies. Many thanks also for my life-coaching grandfather Tibor and encouraging grandmothers Zorka and Marie. Moreover, special thanks go for my soulmate Monika, cousin Michal, classmates & close friends (Lulu, Kikina, Džony, Helena, Katarína, Ina and Michal)!

This accomplishment would not have been possible without you all! Thank you again.

CONTENT

1 INTRODUCTION

Diamond nanoparticles, also known as nanodiamonds, are more and more attractive in many biomedical applications due to their unusual combination of properties. Diamonds also retain the mechanical properties in nanoscale. Moreover, NDs show unique optical properties, excellent biocompatibility and non-toxicity. Commercially available NDs contain nitrogen impurities from the production. After high energy irradiation with subsequent annealing fluorescent NV^- centres are formed. These centres are the origins of the NDs fluorescence, with an emission maximum at circa 700 nm. Due to the nonbleaching and nonblinking fluorescence, biomedical imaging applications using NDs are very promising.

Furthermore, the surface of the NDs can be modified. Polymer coating usually protects the NDs and increase their stability even in the environments with a higher concentration of salts. Various functional groups can be introduced to a polymer shell surface, most notably alkyne or azide groups are interesting because they can be further employed in biorthogonal Copper(I) - catalyzed azide-alkyne cycloaddition (CuAAC - click reaction). *Via* CuAAC click it is possible to attach various molecules to the ND surface, i.e. targeting molecule.

Sentinel node(s) mapping is one of the promising approaches for breast cancer diagnosis and treatment. Sentinel lymph node is the first node nearby to cancer cells. Removal of this node can be beneficial for breast cancer stage diagnosis and for decreasing the chances of remission. The current techniques for sentinel node visualization are employing either radiotracers or blue dyes which are locally injected around the tumour. These are subsequently transported by the lymphatic system into the node(s) and provide contrast necessary for the identification. Both these techniques are clinically used, but they are not sensitive enough to visualise micrometastases and tumour residues.

For successful sentinel node visualization using NDs, the efficient retention of the nanoparticles in the node is crucial. In this case, passive retention using macrophages can be a good solution, because macrophages are gathered in the lymph nodes. Moreover, mannose-macrophages targeting is one of the well-known working targeting strategies.

The main aim of my thesis is to prepare D-mannosylated polyglycerol coated fluorescent nanodiamonds for sentinel node(s) visualisation. Stable fluorescent NPs should be the result of the thesis, and these particles would be further evaluated *in vitro* and *in vivo*, because of their possible application as fluorescent probes for intravital diagnostics and image-guided surgeries.

2 THEORETICAL PART

2.1 Intravital diagnostics

Breast cancer is one of the most commonly diagnosed cancer types, and it is the most frequent cause of death in females around the world. From all cancer cases, breast cancer represents 25 % and 15 % of all deaths caused by cancer [1].

At the beginning of the 1990s, Morton with his colleagues started to work on intraoperative lymphatic mapping in early-stage melanoma, and they explored it by sentinel node visualization which could be possible to detect early metastasis, removal of the sentinel node(s) could be, therefore helpful [2]. The results of the research were later confirmed by Krag and Giuliano [3][4]. Sentinel node (SLN) is the first draining lymph node which receives lymph directly from an organ, and it is also the location where cancer cells are most likely to spread [5].

Macrophages, the immune system cells (among other cells), have access to lymph and they are usually expressed in peripheral lymphoid organs including lymph nodes. Macrophages are important because of phagocytosis, secretion of cytokines and antigen transport [6]. Macrophages can be divided by location to the sinus resident macrophages which are directly connected with lymph and parenchymal macrophages found in the T cell zone, B follicles and medullary cords. Both subcapsular sinus macrophages (SSM) and the medullary sinus macrophages (MSM) are involved in lymph node pathogen capture and retention. Therefore they prevent systemic infections [7]. This process is possible due to the different receptors which are present on the macrophage surface. SSM express number of receptors. However, for us are important CD206 (Mannose Receptor) and CD209b (SIGN-R1) which bind various molecular patterns associated with pathogens. MSM have been shown to effectively clear various nanoparticles, bacteria and apoptotic cells due to their intense phagocytic behaviour [8]. SSM and MSM also differ in the phenotype SSM are defined as classically activated, connected with Th1 type immune reaction, and MSM are associated with Th2 type immune reactions or tolerance [9].

Sentinel nodes mapping has become more widely used in the past decade. Fluorescent intraoperative dyes are employed in these applications. Most widely used agents in the identification of SLN for breast cancer and melanoma surgery are dyes, namely lymphazurin 1 % (isosulfan blue or patent blue V; PBV), methylene blue (MB) [10] and Evans blue (EB) [11]. Also, 5-aminolevulinic acid (5-ALA) and radiotracers (for example, 99mTc-labeled sulfur colloid) are also employed in the SLN mapping. Structures and properties of some mentioned dyes are shown in Figure 1. All these agents have been approved for clinical use by the Food and Drug Administration (FDA), but there are some disadvantages [10]. Allergic reactions have been observed in the case of a visualization using the dyes. Furthermore, blue dye detection is significantly dependent on a surgeons' experience. Hand-held gamma probe guidance system makes surgeons navigation better. Therefore, radiocolloids are commonly added to the blue dye to increase the sentinel node identification rate during the evaluation of breast cancer patients, and the results of imaging are quite successful. However, application of the radiotracers is limited mostly because of the high price [10], [12].

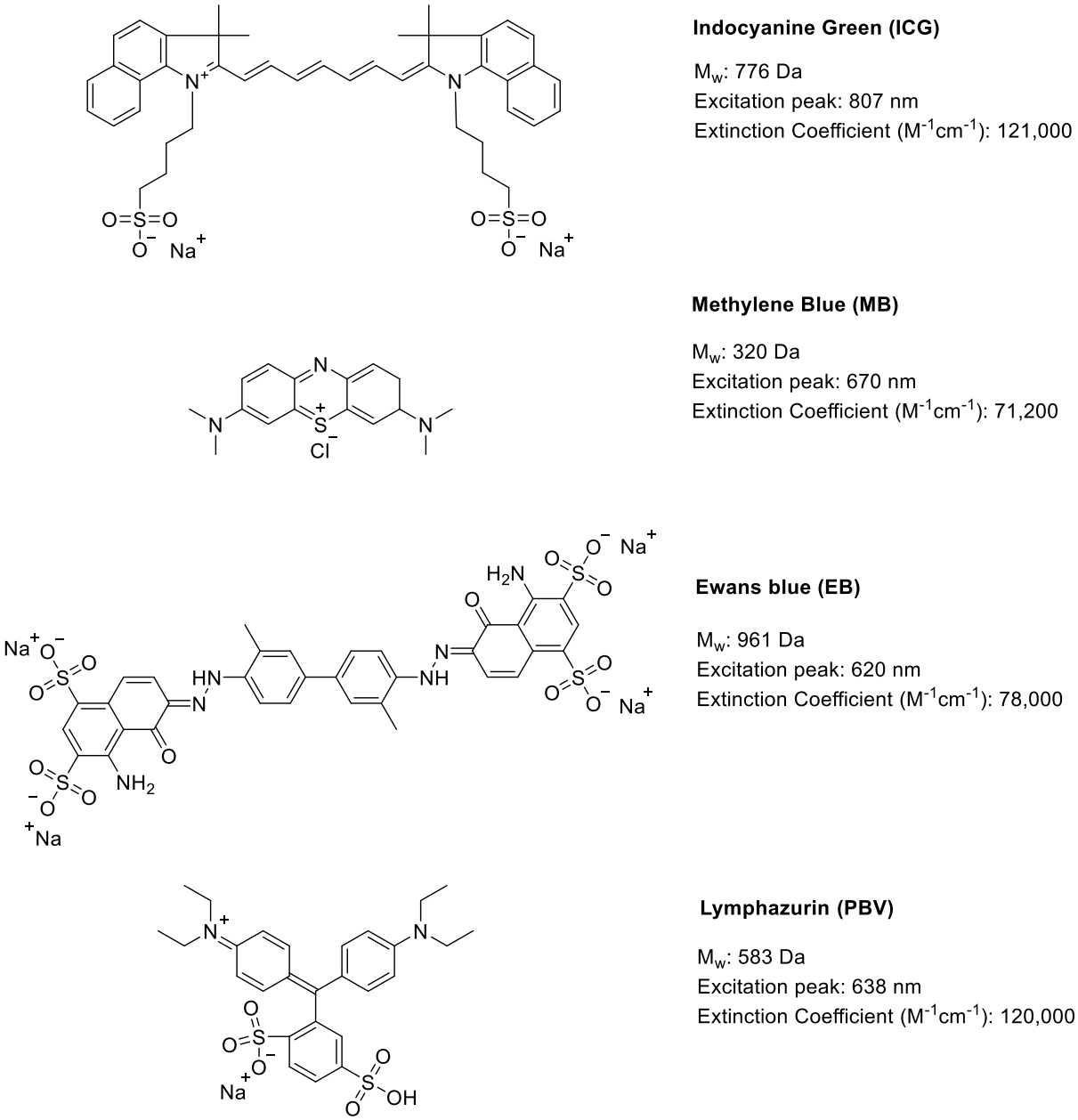

Figure 1 Examples of clinically used blue dyes and their properties [10], [11]

Indocyanine green (ICG; absorption 765 nm, emission 840 nm) became more widely used among blue dyes that are approved by FDA. Visualisation technique using this dye enables us to identify fluorescence emitted from dye that is accumulated in SLN and the fluorescence signal can be seen on a monitor in real-time even through the skin. The allergic reaction for intravenous injection was observed with an overall rate of 0.34 %. The dosage of ICG is lower, and the identification rate is higher than in the case of blue dyes. This method improved common blue dye methods, but the combination of ICG with 99mTc-radiocolloid is still more efficient. All of these limitations lead to the need of further development of alternative methods for these purposes. The most promising future agents are high-intensity fluorescence probes or magnetic tracers with possible magnetometer guidance [10]. Standard SLN visualization methods and future possibilities are schematically shown in Figure 2.

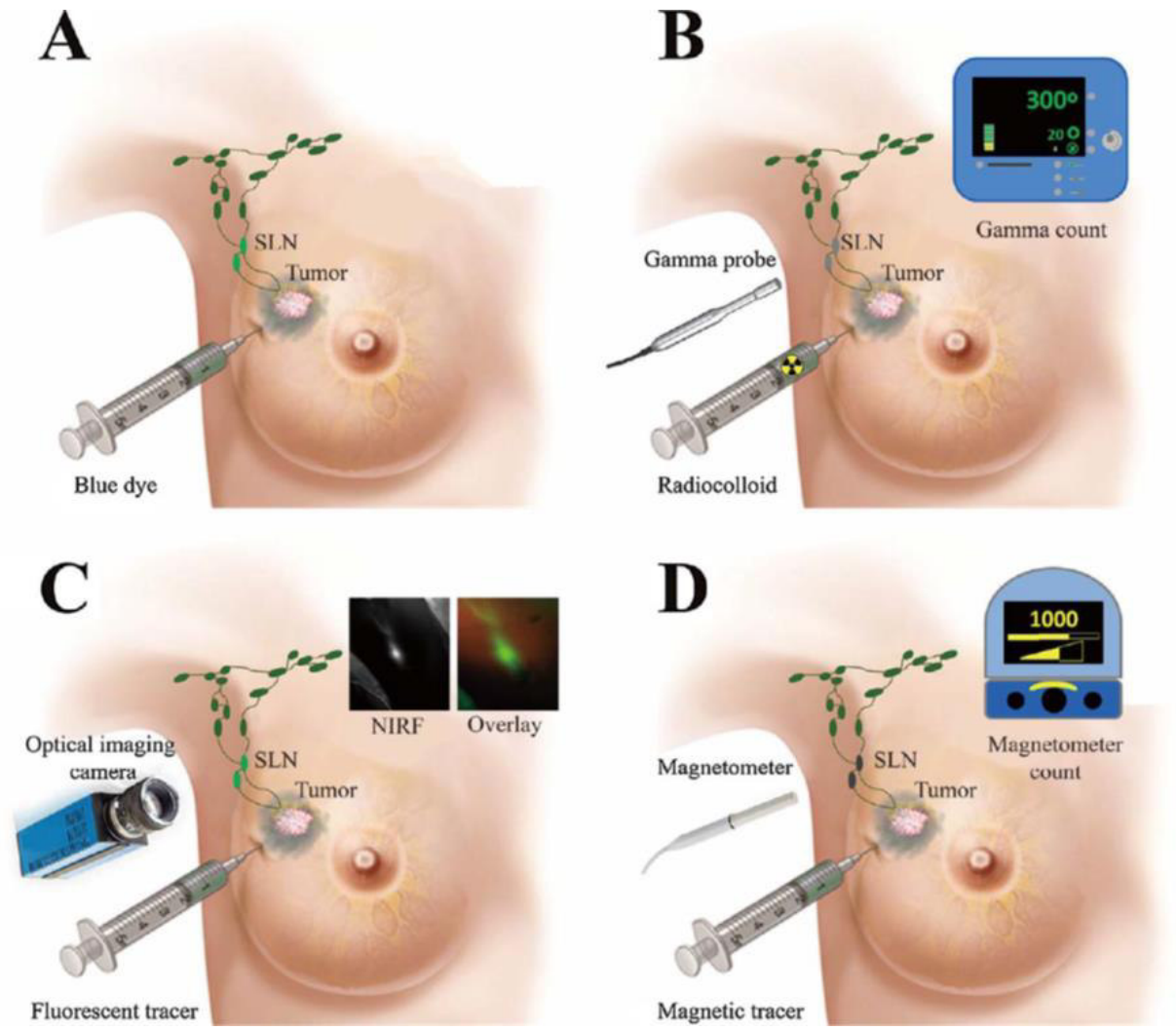

Figure 2 Current standard SLN visualisation methods (A, B) and novel methods (C, D) (picture adapted from lit) [12]

The tumour-specific signal has to be distinguishable from the nonspecific signal of the surrounding. The nonspecific background signal can be induced by intrinsic fluorescence referred to as autofluorescence [13]. With increasing autofluorescence, the TBR (tumour to background ratio) is decreasing. Therefore autofluorescence is the most limiting factor in optical imaging applications *in vivo* [14].

An optical imaging system is required for intraoperative image-guided sentinel node mapping. Some camera systems have been approved by FDA. These camera systems contain two light-sources, optical lenses, filters and detectors. These two light sources enable simultaneous projection of white light image (corresponding to tissue; normal colour texture) and fluorescent image (excited fluorescent tracers). Fluorescent and white light is collected by charge coupled detectors (CCD) and produce a final image [10].

In general, an optical probe for fluorescence imaging consists of a fluorophore and targeting molecule which should not be influenced by the fluorophore. The goal of a targeting (attaching targeting molecule) is to prolong circulation and localise nanoparticles at the site of interest. Fluorophore also should not change the biodistribution of the probe. For clinical applications, parameters such as wavelength, quantum yield, photobleaching, solubility, clearance

and toxicity are crucial. The most efficient wavelength is the NIR region because the maximal tissue penetration is possible and the autofluorescence of tissue is limited. Quantum yield is equal to the number of photons emitted divided by number absorbed photons. The maximum quantum yield is obtained when every absorbed photon is emitted, and it equals 1. Photobleaching describes a permanent decrease of fluorescence as a result of photochemical damage to the fluorophores and can happen when photobleaching threshold specific for each dye is reached [15].

The stable fluorescence and high quantum yield of the agent are needed for minimising applied dose. The maximum concentration of the used dye is limited because of internal absorption, and occurrence of intramolecular fluorescence quenching [16]. The ideal fluorescent probe for the sentinel node imaging should have the appropriate size for travelling through the lymphatic system, but also for retention in the sentinel lymph node long enough. The probe should be cleared rapidly, preferably through renal clearance. Protein binding is also unwanted. Moreover, from a practical point of view, the fluorescent probe has to be nontoxic and soluble [15].

Nanodiamonds are nano-sized particles characteristic by their extreme mechanical hardness combined with interesting optical properties and innate biocompatibility. According to the mentioned properties, FNDs attract attention in imaging applications [17]. The origin of red fluorescence is hidden in an NV^- centres, which can be artificially created (thanks to nitrogen impurities content) using high-energy irradiation and subsequent annealing. The fluorescence maximum of NV^- centres is in the near infrared region, at ~700 nm [15], [16] where the autofluorescence, optical absorption by tissue and active biological environment light scattering are minimised [17].

Moreover, the FNDs fluorescence is stable (without photoblinking), resistant to the photobleaching and has a long lifetime. NDs of different sizes were used for *in vitro* toxicity evaluation. The investigation proved that NDs are non-cytotoxic with no effect on proliferation, protein biosynthesis, cell differentiation, cell cycle and cellular morphology. *In vivo* NDs behaviour is different depending on the injected dose and NDs surface modification, but previous research shows up that safety of NDs is satisfactory in small dosages [15], [18].

2.2 Preparation of NDs

Nowadays, various methods of nanodiamonds production are known, including “static” high-pressure high-temperature method (HPHT), “dynamic” detonation synthesis and laser ablation. All of these are commercially available. In addition to the commercial methods, nanodiamonds can also be prepared by chemical vapour deposition, microplasma-assisted atmospheric pressure NDs forming from ethanol vapour, ultrasound cavitation, carbides chlorination and graphite ion irradiation. HPHT NDs and DNDs follow different NPs preparation approaches: top down vs bottom up. During the top-down process, smaller particles are obtained from the bigger ones (HPHT micron diamonds milling), while the bottom-up approach follows nanoparticles synthesis (detonation synthesis). Based on the used preparation method, NDs show different properties, which results in possible usability for different applications [19].

2.2.1 High-pressure high-temperature method

Diamond crystals sized up to a few mm can be produced using the HPHT method. The commercially available HPHT NDs powder is produced by ball milling of bigger HPHT NDs (smallest average size obtained is 20 nm). These particles have an irregular shape and sharp edges. Requirements for the successful graphite powder conversion during the HPHT process: pressure approx. 6 GPa and the temperature 1,500 °C with metallic catalysts. These conditions must be stable for 50 - 100 h, sometimes even longer. The temperature and pressure values correspond to used precursors in synthesis and type of catalyst [20]. When for example fullerenes are converted to diamonds, the synthesis conditions are 5.0-5.5 GPa and 1,400 °C [21], for carbon nanotubes conversion NiMnCo catalyst is used, the pressure is 4.5 GPa, and the temperature is 1,300 °C [22].

2.2.2 Detonation method

The detonation method was developed in the 1960s in the former USSR [23]. Particles of 4-5 nm primary size are produced by the firing of carbon-containing explosives in detonation chamber, as byproduct metallic impurities are obtained. Typically the mixture of hexogen with TNT (ratio 40:60) of C, N, O, H composition with negative oxygen balance (resulting in the presence of nonoxidised carbon) is used. During the explosion the inert conditions are maintained, we distinguish the "dry" or "wet" synthesis according to using gases (N_2, CO_2, Ar) or water (ice), respectively. During the synthesis, the detonation soot or diamond blend with 40-80 wt % diamond phase (depending on conditions) is obtained [19].

During the initial shock, the chemical decomposition is caused by the high-explosive material compression at high temperature. The free carbon is formed according to the following scheme (1):

$$CNOH - - \rightarrow N_2 + H_2O + CO + CO_2 + C \quad (1)$$

The decomposition end occurs at the specific value of pressure and temperature, called Jouguet point, which is located in the liquid carbon region (of a nanocarbon phase diagram) for the powerful explosives. During the first 1 ns explosive molecules decomposition occurs, in next 10 ns primary carbon nuclei are formed (size less than 2 nm). Next stage is the primary embryos coagulation into carbon droplets (bigger than 2 nm) at 16.5 GPa or more, during the time 100-1,000 ns after synthesis. The final step is a crystallization of the carbon droplets which lasts more than 1,000 ns at a pressure ranging between 9 and 16.5 GPa [19].

2.2.3 Chemical vapour deposition

Another example of NDs preparation is chemical vapour deposition (CVD). This method allows direct nucleation and growth of nanodiamond powder from the vapour phase. Nucleation and NDs growth at low-pressure conditions in a microwave plasma CVD reactor (without substrate) use were studied since late 80s. The process starts typically by plasma activation of methane in a mixture with hydrogen forming C_xH_y radicals. The flow of the formed radicals continues by diffusion and convection to the diamond surface. The diamond structure grows thanks to the chemical reactions between the flow and surface. The substrate surface can be seeded with NDs particles or not. In the first case (epitaxial growth) the natural or HPHT diamonds are used as nucleation centres. Another approach without seeding (heteroepitaxial) require minimal

diamond-substrate mismatch because spontaneous nucleation is almost impossible on foreign substrates. This process takes place in microwave plasma CVD reactor at low pressure [24]. The high purity homogenous nucleated nanodiamond particles with spherical-like morphology can be prepared with an average particle size circa 50 nm. The particle size can be increased by presence of heteroatoms. For instance, diborane addition leads to particles, up to 450 nm in diameter [19].

2.2.4 Laser ablation

Another approach for nanodiamond production is a laser-assisted method using a graphite target in a liquid medium – water/acetone at room temperature and atmospheric pressure [25]. The ND formation occurs most likely due to the present extreme temperature and pressure conditions. The first step during the process is the explosive decomposition of the target surface region, then, the vapour and clusters are ejected to the liquid region, this cloud is mixed with the liquid which is boiling or exists in the supercritical state followed by growth and solidification of NDs at fast-quenching conditions. The final size corresponds to the heat and mass transfer during the whole process [20].

2.3 Optical properties of FNDs

Heteroatoms incorporated into the diamond lattice can make NDs optically active (fluorescence origins). The most frequently occurred impurities incorporated in NDs structure are nitrogen atoms. There are heterogeneously spread nitrogen atoms in the raw industrial HPHT NDs. Growth conditions and internal diamond structure strongly influence nitrogen distribution [19].

There are several forms of the nitrogen states in NDs, which are single substitutional nitrogen-N_s (P1 centre); two neighbouring embedded nitrogen atoms (A-center), the charge-neutral nitrogen-vacancy centre NV^0; the negatively charged nitrogen-vacancy centre NV^- [26]. Schematic representation of NV^- centre is shown in Figure 3 and NV centres photoluminescence properties in Figure 4.

HPHT nanodiamonds can be divided into several groups according to nitrogen impurity concentration and state. The substitutional state of nitrogen impurities (N_s) is abundant in HPHT NDs Ib type at concentration 100-200 ppm. The lower quality NDs type Ib with nitrogen content up to 400 ppm are commercially available too. The NDs type Ia are produced by natural diamond milling and contain nitrogen as A centres (nitrogen in the aggregated state) up to 3,000 ppm [26].

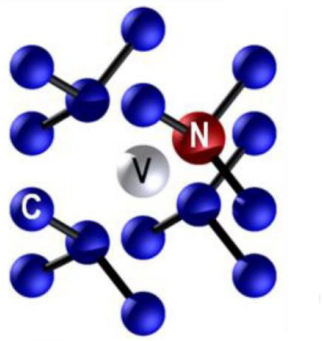

Figure 3 Schematic representation of nitrogen-vacancy NV^- center. "V" stands for vacancy (picture adapted from lit.)[27]

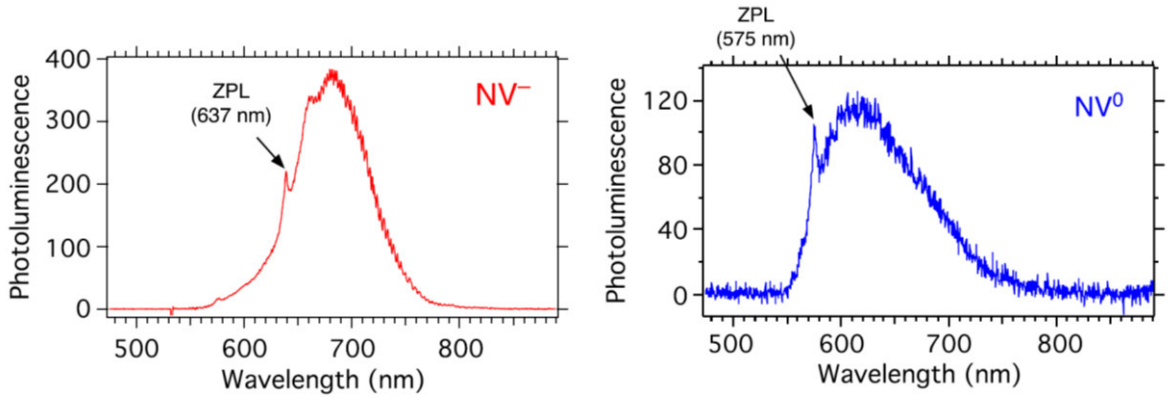

Figure 4 Photoluminescence spectrum of the single NV^- centre (red) and NV^0 centre (blue) at room temperature, laser excitation 532 nm (picture adapted from lit.)[28]

When HPHT NDs of type Ib are subjected to high-energy irradiation. The high energy particle beam is capable of displacing carbon atoms and thus creating vacancies. During the following annealing process, the nitrogen-vacancy NV colour centres with red emission are formed. The annealing treatment allows vacancies to migrate closer to the nitrogen impurities, and then the recombination of vacancies with nitrogen atoms occur (centres are stable) [28] (Figure 5). In the case of type Ia NDs, green luminescence due to NVN (H_3) centres formation is observed after irradiation and annealing [29]. DNDs are not suitable for this kind of applications due to major nitrogen impurities in an aggregated state (A centres), which make the diamonds optically inactive even after irradiation and annealing. Moreover, photoluminescence of the NV centres, in the case of smaller DNDs, is not so stable [26].

2.3.1 NV centre creation

The NDs are subjected to the high energy irradiation (p^+, He^+ or e^-; a few keV to a few MeV) leading to the displacement of interstitial carbon atoms from their positions forming vacancies. The selective production of NV^- centres (not neutral ones) from neutral vacancy V^0 was demonstrated in the Ib HPHT diamond type by two-step mechanism according to the following scheme (2):

$$V^0 + 2N^0 \rightarrow NV^0 + N^0 \rightarrow NV^- + N^+ \qquad (2)$$

If the nitrogen impurity level is around 100 ppm, we can obtain a concentration of NV^- centre ca 50 ppm (roughly 50 % conversion). At nitrogen concentration 10 ppm, production of NV^- was not observed [28], [30].

The mass method capable preparation of NDs with the largest concentration of NV centres is important corresponding to the brightest particle production for biomedical applications. The FNDs can be prepared from commercially available nanocrystals by direct irradiation and following annealing. Another approach is irradiation and annealing of micron-size HPHT diamonds which are subsequently milled into nanocrystals. Larger NDs have a higher probability than the smaller ones to obtain more intensive fluorescence in a single particle. During both procedures, sp^2 carbon phase impurity is formed at the NDs surface and needs to be removed. Due to the sp^2 carbon impurities the luminescence properties of NV^- centres cannot be visible (sp^2 absorption interfere with both excitation and emission wavelength) [28], [30].

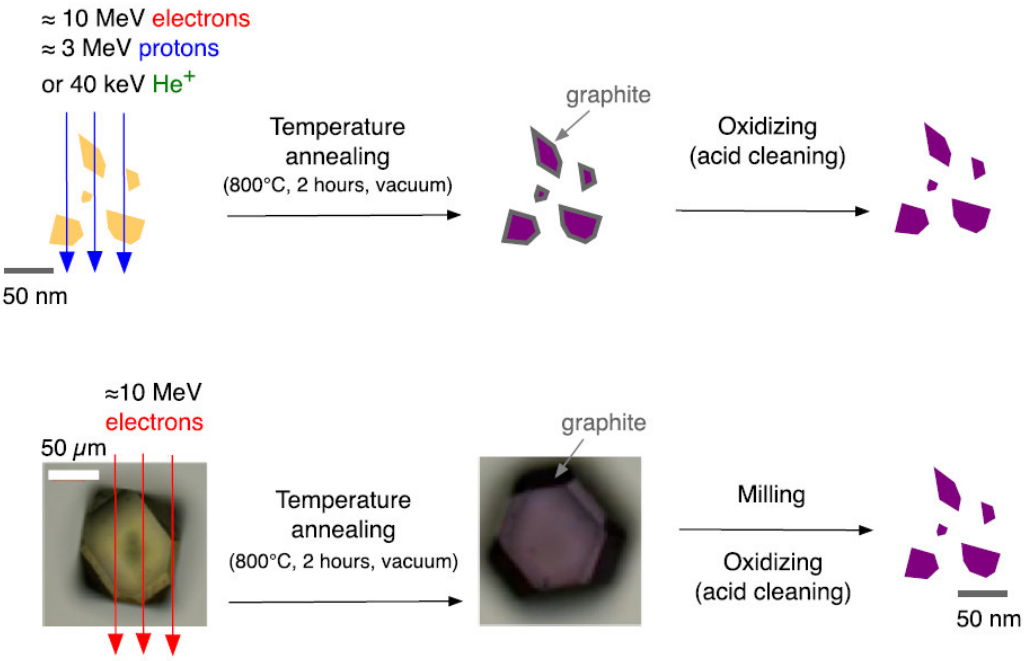

Figure 5 Two possible ways to create NV centres (picture from lit.) [28]

2.4 Surface chemistry of NDs

As it was mentioned above, different approaches are used to produce NDs. Commonly the surface of commercially available NDs is oxygenated. Purification steps are necessary for the next modification purposes. Usually, NDs purification is performed using air oxidation at high temperatures and/or mineral acids treatment. The carbonyl and carboxyl group surface enrichment is the result of this oxidation procedure. The sp^2 surface impurities, as well as isolated double bonds, π-conjugation areas, graphene-like or graphitic structures, are also removed during this process. Due to the different surface nature, the values of zeta potential are ranging between – 50 to + 50 mV. Negative potential values are typical for the carboxylated surface [31].

2.4.1 Hydrogenation

From the structural point of view, the hydrogenated diamond surface is the simplest, using CVD method of diamond preparation in a hydrogen atmosphere this kind of nanodiamonds can be directly prepared. Normally, the surface contains also functional groups with oxygen, and it is necessary to replace these groups completely. The common reducing agents are not able to convert all oxygen-containing groups into the pure hydrocarbon, so the hydrogenation conditions are rather harsh. One of the hydrogenation procedures is thermal hydrogenation at 850 - 900 °C; Other commonly used one is in plasma with a hydrogen atmosphere. After thermal treatment, several alcohol groups remain on the diamond surface. Another approach is employing metal catalyst (Pd, Pt, Rh or Ni) during the reaction (low reactivity is frequently associated with high association barrier). Molecules of hydrogen are broken, using hydrogen plasma, and reactive species interact with a diamond surface in a reductive manner. Diamond surface termination homogeneity can be higher if the hydrogenation is repeated and the sample is thoroughly mixed during the process [31]. Hydrogenated NDs preparation possibilities are shown in Figure 6.

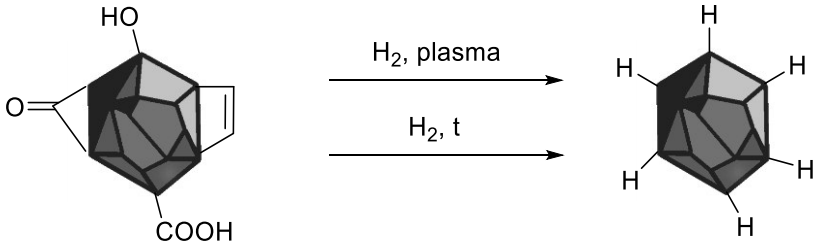

Figure 6 Schematic representation of hydrogenated NDs preparation (adapted from lit.) [31]

2.4.2 Hydroxylation

There are two possibilities for hydroxylated NDs preparation – oxidation and reduction. Several techniques for this kind of modification exist for example ketones and acids reduction using boranes [31]. The reaction success is strongly dependent on lactones and esters content, which are not easily converted to hydroxyl groups using the borane. The advantage of borane is possible hydroboration of sp^2 carbon impurities (unsaturated moieties reduction). Highly reactive hydrides such as $LiAlH_4$ are used in reduction reactions [32]. Inorganic compounds from the sample can be removed by a combination of hydrochloric acid treatment with appropriate complexing agent (e.g. citrate). Hydroxyl groups can be introduced onto the NDs surface by a photochemical generation of OH radicals in situ. OH, radicals can be synthesised chemically using an acidic mixture of $FeSO_4$ and hydrogen peroxide (Fenton – oxidizing agent) [33]. Hydroxylated NDs preparation possibilities are shown in Figure 7.

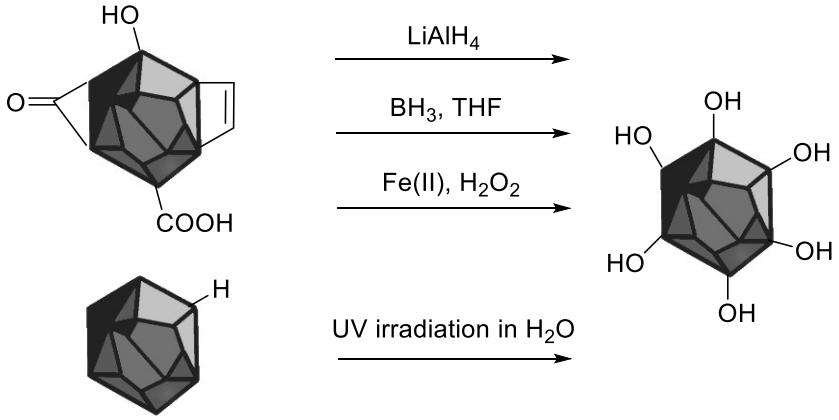

Figure 7 Schematic representation of hydroxylated NDs preparation (adapted from lit.) [31]

2.4.3 Carboxylation

The carboxyl and keto groups represent one of the highest oxidation states of the carbon. We distinguish two different oxidation pathways – dry oxidation and wet oxidation. Dry oxidation using air or oxygen to control sp^3/sp^2 ratio on the diamond surface [34], [35]. The temperature ca 400 °C is necessary for oxidation onset, but at higher temperatures than 450 °C all kinds of nanocarbon materials oxidize. At the narrow temperature range around 425 °C only sp^2 carbon can be selectively burned, and the oxygen-containing functional groups are being formed on the resting NDs surface [31], [35]. sp^2 carbon removal is crucial in the case of fluorescent nanodiamonds because fluorescence properties are improved. After such treatment, the diamond surface contains -COOH groups, but many hydroxyl groups and other oxygen-containing functional groups are also present. Higher temperatures were also used for this purposes, but the higher oxidation temperature is, the larger is the NDs weight loss [31].

The dry oxidation can be followed by wet oxidation. The wet oxidation agents are mineral acids mixtures containing i) HNO_3, H_2SO_4 and $HClO_4$; ii) HNO_3, H_2SO_4 and HCl, in equal ratios and oxidation is carried out at high temperatures up to 200 °C. Another approach is oxidation using a mixture of hydrogen peroxide with sulfuric acid also known as "piranha solution" [36] or pure hydrogen peroxide, or a 3:1 mixture of concentrated sulfuric and nitric acid [37] (Figure 8). These strong oxidation conditions lead to surface purification thanks to sp^2 carbon removal. This is caused by the different oxidation behaviour of sp^2 carbon in comparison with sp^3 carbon [38]. However, it should be noticed that this treatment is accompanied by significant diamond weight loss. Supercritical water is another of the strong oxidation agents which can selectively oxidize nondiamond components. Mineral acids and also supercritical water can also remove other impurities such as metal impurities, because of the solubilization [31].

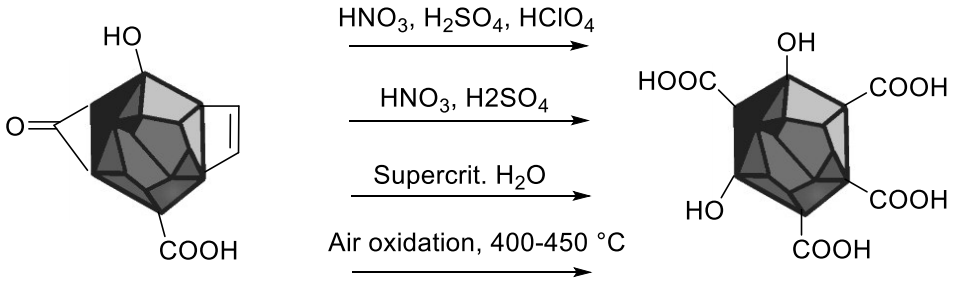

Figure 8 Schematic representation of carboxylated NDs preparation (adapted from lit.) [31]

2.5 Polymer Coating

The high stability of NDs in water, buffers and other kinds of solutions with high ionic strength is necessary for all biomedical applications. Moreover, reduced nonspecific binding of biomolecules and particle charge changes are necessary. One of the approaches which can increase NDs stability is hydrophilic polymer coating. There are numbers of polymers which can be used for these purposes (Figure 9). These polymers ensure the stability of NDs by electrostatic or steric repulsion, which protects the NDs against their contact and possible aggregation [39].

One of the most famous synthetic polymer used for polymer coating is poly(ethylene-glycol) (PEG) and its derivatives. Many PEG modifications were developed, for example poly(PEG-methyl ether methacrylate) (PPEGMA), poly[N-(2-hydroxypropyl) methacrylamide] (PHPMA) or poly[2- dimethylamino)ethyl methacrylate] (PDMAEMA), or poly-(N-isopropylacrylamide) (PNIPAM) [40].

Multi-branched poly(glycerol) (PG) layer is also one of the coating possibilities. The advantage of the PG layer is higher density due to branching in contrast with the PEG layer formed by linear polymer chains. Moreover, PG coating attracts attention in biomedical applications due to antifouling effect, long plasma half-lives and prolong circulation (besides the biocompatibility and hydrophilic properties) [41].

Other synthetic polymers, such as poly(ethylene-imine) (PEI) [42], poly(allylamine hydrochloride) (PAH) [43], have been also tested for polymer coating.

Natural polymers such as polysaccharides, proteins and nucleic acids can also be used for NDs coating. It has been reported that proteins such as human serum albumin, bovine serum albumin and silk fibroin stabilize NDs. Among polysaccharides, dextran was used for these purposes [44].

We distinguish two coating possibilities: non-covalent adsorption employing hydrophobic or electrostatic interactions and covalent modification, which further divides into "grafting to" and "grafting from". During "grafting to" approach synthesised polymer is attached to the ND surface in comparison with the "grafting from" strategy where polymer grows directly from the ND surface. The main advantage of non-covalent surface modifications is that they are experimentally simple. However, it should be noticed, that using covalent attachment leads to stronger connections in comparison to non-covalent approach [39], [44].

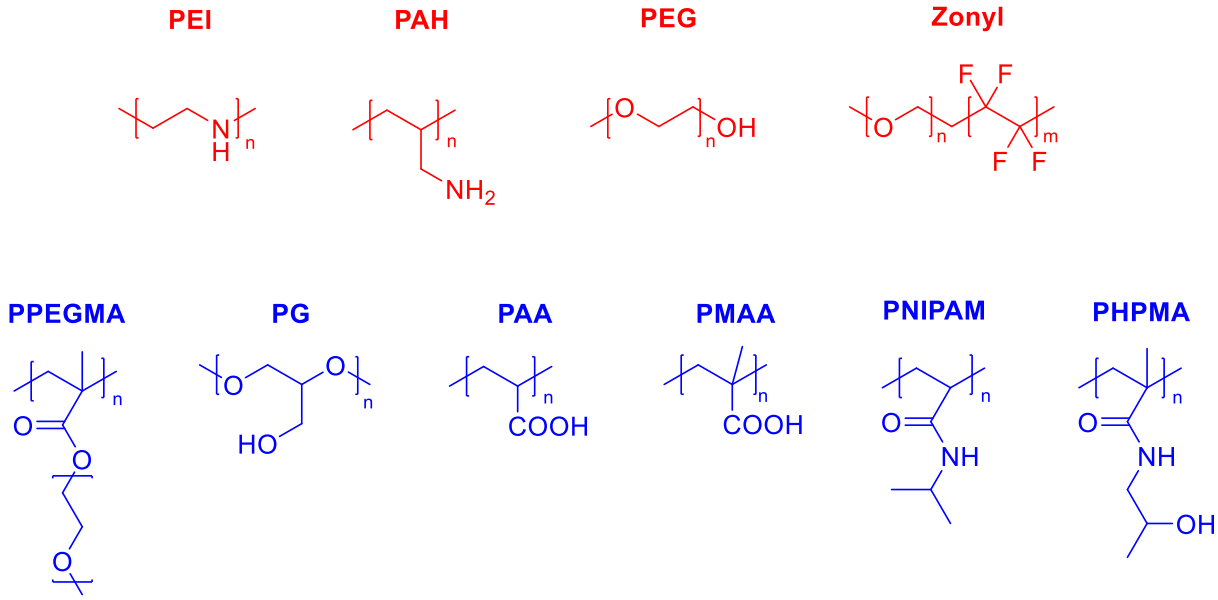

Figure 9 Structures of polymers which have been used for covalent polymer coating of NDs; "grafting to" (red) and "grafting from" (blue) (picture adapted from lit.) [39]

2.5.1 Non-covalent modification

NDs surface modification with block copolymers is possible, i.e. due to the hydrophobic interactions. Usually, one block is attached on the surface as an anchor, and the other block is almost without ND affinity.

Some polymers with a positive charge such as PEI or PAH can adsorb onto surface ND, due to the electrostatic interactions. Amount of adsorbed polymers varies with the colloidal stability of NDs. This kind of modified NDs is formed during sonication by slow addition of one substance to the other.

Carboxylated NDs show affinity for biomolecules including enzymes, peptides, antibodies and other proteins. The protein-adsorption is possible due to the electrostatic interaction of ND's surface containing carboxylic groups ($-COO^-$), and positively charged amino groups ($-NH_3^+$) present in proteins and hydrogen bond is often also formed [39].

2.5.2 "Grafting to"

"Grafting to" approach utilizes polymers with a reactive group on one end of the polymer, which forms a bond to the ND surface (most cases ester or amide bond). Further modifications with biomolecules are possible if other biorthogonal groups are present. Many kinds of these particles were prepared for drug delivery and/or targeting [45], [46], [47]. NDs after the modification are more stable in PBS and nonspecific protein binding in FBS decreases [48].

Polymers can be attached to the surface in various conformations according to architecture and density of the polymer layer. If polymer coils are well separated, formed conformation is called „mushroom". Higher concentration of overlapping polymer coils form „brushes". Steric hindrance is one of several limitations of "grafting to" approach. The polymers have to diffuse through the layer to form a bond with functional groups on a ND surface [44].

2.5.3 "Grafting from"

"Grafting from" approach is used in many different types of ND surface polymerisations such as widely-used radical living polymerization. The advantage of the living polymerization is that polydispersity, brush thickness and composition is controllable [44]. Polymers containing different functional groups such as alkynes, azides, can be used which further enables polymer modification [49].

One of the working strategies, how to prepare stable NDs is PHPMA polymer grown on the terminal methacrylate groups of thin silica layer. This approach represents conventional radical polymerization and it is carried out at presence azobisisobutyronitrile (AIBN) as thermolabile radical initiator. Next example is copolymerization of 3-(azidopropyl)methacrylamide with PHPMA, which further extends bioorthogonal modification possibilities. These particles were stable in 1 M NaCl, and non-specific protein binding was significantly reduced. NDs prepared by combination of PHPMA and tripeptide Arg-Gly-Asp (RGD) show potential in cancer cells targeting [50].

The polyglycerol layer can also be grown on NDs surface using non-radical ring-opening polymerization (acid catalyzed – by functional groups on the surface). This coating is increasing NDs stability and reducing non-specific protein binding. PG layer can extend further applications for example modifications via CuAAC click reaction because terminal –OH groups can be replaced by azide groups. Using this reaction, RGD peptide can be attached, and cancer cell targeting was also enabled as in the case of PHPMA coating [49].

"Grafting from" strategy also includes two reversible-deactivation radical polymerization types specifically - atom transfer radical polymerization (ATRP) and reversible addition-fragmentation chain transfer (RAFT) polymerization [51], [52]. Halide terminated NDs can be polymerized by. hydrophobic poly(tert-butyl methacrylate) or PMMA. Employing a similar strategy, 2-(dimethylamino)ethyl methacrylate (DMAEMA) monomer can be "grafted from" too [51]. The first step in RAFT polymerization is the introduction of a chain transfer agent (CTA) to NDs surface. CTA-NDs were polymerized with poly[poly(ethylene glycol) methacrylate] (PPEGMA) monomer using AIBN as radical initiator [52].

2.6 Click chemistry

„Click chemistry" is quite a new approach of reactions which are modular, wide in scope, give very high yields, generate only inoffensive byproducts (can be removed without using chromatography) and they are stereospecific (not necessarily enantioselective). Characteristic requirements for the reaction are simple reaction conditions (ideally, insensitive to oxygen and water), readily available starting materials and reagents, water as a solvent, and simple product isolation. Non-chromatographic methods for purification are crystallisation or distillation, and the product must be stable under physiological conditions [53].

We distinguish many carbon-heteroatom bond forming click reactions. The "classic" CuAAC click is until now one of the most famous click reactions [54]. In classic CuAAC click, the reaction uses Cu (I) as a catalyst of the 1,3-dipolar cycloaddition of an alkyne group with an azide to form a 1,2,3-triazole [55].

During the reaction, it is necessary to maintain a high concentration of Cu(I), which makes the reaction possible. Usually, Cu (II) salt commonly ($CuSO_4$) is used as pre-catalyst in the presence of a reducing agent – sodium ascorbate [55]. Appropriate ligands are used in the click reaction to stabilize Cu(I) during the reaction and also to protect biomolecules from oxidation [56], [57]. Copper and sodium ascorbate are damaging for the biological and synthetic polymers; during the reaction the reactive oxygen species are generated by copper, and also ascorbate byproducts (as dehydroascorbate and others) can oxidize guanidine (arginine) and amino groups (lysine) leading to protein aggregation. Aminoguanidine is known to capture reactive oxygen compounds while not influence significantly the reaction rate [56]. Most commonly used ligands are from a family of tris(triazolylmethyl)amine: THPTA, BTTP and BTTPS [56], [59]. The structures of ligands are in Figure 10. BTTPS show better acceleration effect in CuAAC click reaction in vitro, but it has lower labelling efficiency of modifying significantly negative molecules because of electrostatic repulsions [59].

Usually Cu(II) salt with the ligand is premixed and subsequently added to the azide, alkyne substrates. The last reactant added to the mixture is sodium ascorbate (reaction initiator) [56]. The reaction should be also buffered; compatible buffers are phosphate, carbonate or HEPES-(4-(2-hydroxyethyl)-1-piperazineethanesulfonic acid) in the pH range from 4 to 10 (pH 7 is recommended in most cases) [56], [57]. Tris buffer is not recommended because the tris(hydroxymethyl)aminomethane molecule inhibits the reaction by chelating the Cu. In some cases, an increasing reaction temperature or solubilizing agents such as DMSO addition can be helpful [57]. The most probable click reaction mechanism is showed in Figure 11.

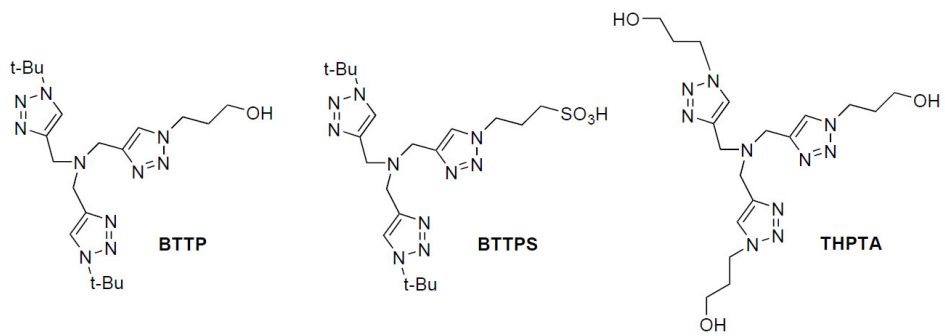

Figure 10 Structures of ligands used for CuAAC reaction

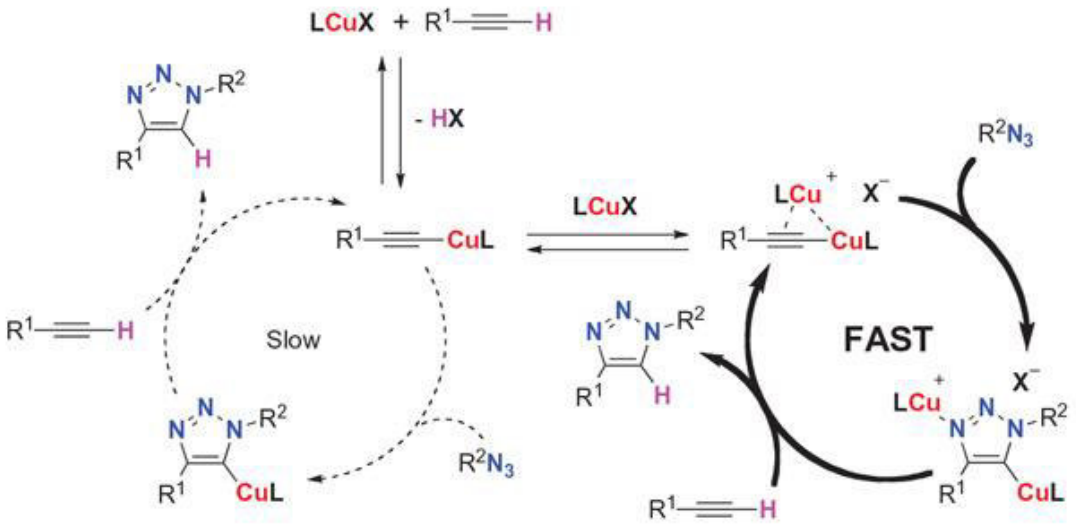

Figure 11 Promising mechanism of CuAAC reaction (picture from lit.) [57]

2.7 Biomedical applications of FNDs

The most important properties are biocompatibility, non-toxicity and chemical stability for all biomedical applications of NDs [60]. Few toxicity studies were performed using fluorescent HPHT NDs *in vivo*. Introduction of fluorescent HPHT NDs into the worms (*Caenorhabditis elegans*) has not shown oxidative stress or shorten life span [61]. Toxicity was also not observed after intradermal administration in the case of mouse and rat model organisms in a period of 5 months [62]. As we know, the stability of NDs can be improved using, i.e. polymer coating thanks to the tunable surface structures on the NDs [44]. Furthermore, NV^- centres, which emit non-blinking and non-bleaching fluorescence with long lifetime (possible detection of biodistribution), are present in the NDs lattice.

These features lead to FNDs applications such as single particle cell tracking [63], long-term tracking of particles *in vivo* [64], tracking of neuronal processes [65], drug/gene delivery [66] and fluorescence lifetime imaging microscopy, both *in vitro* and *in vivo* [67].

2.7.1 Cell targeting and Bio-labelling

Cell targeting is widely used NDs application. The most efficient targeting is when there is a significant difference between the uptake by target cells and other cells, this was observed, for example, between normal and cancer cells [68]. Targeting approach is based on the specific interactions of the modified NDs with overexpressed cell receptors (enhanced NDs internalization into the cells). Different molecules (including hormones, peptides or antibodies) have been utilized for cell targeting [69]. These molecules should be possible to be synthesised on larger scales, they should be biocompatible with the ability to retain a drug at a target site, and they should enhance pharmacokinetic properties and reduce drug toxicity.

FNDs are well suited in ligand-based targeting and antibody-based labelling of mammalian cells. For example, BSA coated high-brightness FNDs were used to reduce non-specific cell binding. These FNDs were further modified with sugar residues and lactose to increase uptake in liver cells. The presence of the conjugates in HepG2 cells was proved by confocal fluorescence imaging [68].

Specific labelling of CD44 antigens on cell surfaces were studied employing antibody conjugated to FNDs. Two human breast cancer cell lines with different expression levels of CD44 were used for comparison of this kind of labelling. Antibodies can bind to extracellular epitopes of CD44 receptors, so the antibodies were modified with biotyne. The used method shows labelling efficiency comparable to conventional approaches employing organic dyes. Particles can be observed by confocal fluorescence microscopy [68].
FNDs based particles (coated with N-(2-hydroxypropyl)methacrylamide copolymer) after conjugation with cRGD peptide was used for efficient and specific targeting of glioma cells *via* integrin $\alpha v\beta_3$ receptors which enhance efficiency of internalization [50].

Next promising application is long-term labelling employing FNDs. FNDs were used to track slow-proliferating cancer stem cells (CDCs) *in vitro.* The FNDs platform could enhance understanding of CDCs chemical properties also *in vivo* [64].

Among different applications, stem cell research *in vivo* includes many challenges. Therefore technique for this application should be robust. Quantum dots have been considered as promising material, but their toxicity is limiting factor in these applications. In vivo study of stem cells using FNDs labelling showed promising results. Stem cells are interesting group of cells which have the ability to self-renew and differentiate. FNDs were used for bio-labelling and tracking of engraftment of transplanted lung stem cells (LCs) in a mouse model. First, in vitro study showed that the labelling does not influence cell-renewal and differentiation properties. The FND labelled LSCs were administered intravenously to the lung-injured mouse. Injected LSCs were searched using fluorescence lifetime imaging microscopy (FLIM) in mouse organs. The labelled cells were determined in lung tissue with single-cell resolution [67].

2.7.2 FNDs as nanoscopic sensors

Furthermore, FNDs show potential also in applications as nanoscopic sensors thanks to the NDs colour centres response to the surrounding. The negatively charged nitrogen-vacancy centres have been used as nanosensors for imaging. The spin properties of NV^- centres are temperature dependent, which enables use of NV^- centres as nanoscopic sensors for local temperature. Besides the temperature also magnetic and electric sensing employing the colour centres in diamond. All of these applications are dependent on the electronic spin of NV^- centres. There is also the response of NV^- centres to chemical processes on the NDs surface. NV^- centre can be directly used to sense mechanical strain – nanomechanical resonators [31]. The fluorescence shape of spectra is changed after surface oxidation and also in the case of charged polymer adsorption [70], [71].

Neuronal activity, cell membrane ion channels and communication between cells could be investigated using NV^- centres in FNDs. Measuring the local temperature of living cells could be possible employing NV^- centres as temperature sensors. However, there are still many technical challenges in these applications [31].

2.8 Methods

We can observe that properties of NPs differ with a change of their size at the nanoscale level. Due to this fact, the size distribution of NPs is one of the crucial parameters to control different nanomaterial properties. One of these properties is chemical reactivity which is dependent on NP surface/volume ratio. Diffusivity and NPs capability to permeate cell membranes are also properties determined by NPs size [72].

There are various methods to characterise nanoparticles. The obtained information can be divided into two groups: physical characteristics – size, shape, size distribution surface area, charge; and characterisation of chemical composition and concentration. Various analytical information about NPs can be obtained using optical methods, which are based on interactions of light with matter, such as DLS. Other methods are those based on interactions with electrons such as TEM [72].

2.8.1 Dynamic light scattering

Dynamic light scattering (DLS, i.e. quasielastic light scattering or photon correlation spectroscopy) is a versatile non-destructive method using elastic scattering to determine particle size and size distribution in colloid solution or suspension.

NPs are randomly travelling through the colloidal solution because they undergo Brownian motion. The light beam (scattered from a laser) interacts with NPs within the sample [72]. During random motion of particles, the scattering centres in the sample are displaced. Based on particle speed during the motion and their size, changes of scattering intensity are observed. In contrast to smaller particles, bigger particles move slower but scatter the light more. Due to the constructive and destructive interferences of scattering by NPs in the sample, scattering intensity fluctuates over time [73].

From the time-dependent fluctuations in light intensity, i.e. from the decay of the autocorrelation function, the average particle size can be calculated [74]. The autocorrelation function has exponential behaviour, and the decay rate of the function is proportional to a diffusion coefficient [75]. The average diffusion coefficient (D) of the particle in solution is related to the hydrodynamic diameter (D_h) of the particle via the Stokes-Einstein equation (3), as follows:

$$D = \frac{k_B T}{3\pi\eta_0 D_h} \tag{3}$$

Where k_B is the Boltzmann's constant ($1{,}38066 \cdot 10^{-23}$ J/K), T is the absolute temperature, and η_0 is the solvent viscosity. Hydrodynamic diameter is a parameter for NPs size description corresponding to a spherical particle with the same diffusion coefficient [72], [76].

2.8.2 Zeta potential

Zeta potential, also known as an electrokinetic potential is alongside the size of NPs a widely used parameter which can be easily measured by light scattering techniques. Zeta potential is the potential at the slipping/share plane of a particle moving in colloid solution as soon as the electric field is applied. The direction and velocity of motion are dependent on electric field, charge and type of dispersant [77], [78]. Slipping or share plane is a hypothetical interface between electric double layer surface and dispersant. The adsorbed double layer (EDL)

is formed on the charged particle when the particle is dispersed. The inner layer of the EDL, named Stern layer, contains mostly ion molecules with the opposite charge in respect to NPs charge. Experimentally the electrostatic effect is present for several nm from NPs surface. Above the Stern layer, the impact of NPs surface charge decreases and electrostatic effects are weaker corresponding to Debye's law. This outer layer of EDL contains both the same and also opposite charged ion molecules. The composition of this part of EDL named the diffusion layer is dynamic and it varies depending on many factors, e.g., pH, ionic strength, concentration, surface charge and colloid stability [77], [78].

Zeta potential describes electrostatic stabilization and sometimes particles are divided according to the values of zeta potential into several groups differing in the stability: particles which tend to aggregate in the range of ± 0–10 mV, minimally stable particles ± 10–20 mV, moderately stable particles above ± 20–30 mV, and highly stable particles are from ± 30 mV (reality is pretty more complex) [77].

During the Zeta potential measurements, an external homogenous field is produced in the measurement cell. Particles move at a constant speed within the sample solution towards the electrodes [79].

Zeta potential is not measured directly, but we can calculate it from the electrophoretic mobility values. Electrophoretic mobility of the NPs is equal to particle velocity V (μm/s) divided by electric field strength E (V/cm) (4)

$$\mu_e = \frac{V}{E} \tag{4}$$

Electrophoretic mobility can also be obtained from Henry´s equation (5):

$$\mu_e = \frac{2\varepsilon_0 \varepsilon_r \zeta f(Ka)}{3\eta} \tag{5}$$

where ε_0 is permittivity of vacuum, ε_r is relative permittivity, f (Ka) is Henry´s function, η is dynamic viscosity (according to measurement temperature), and ζ is zeta potential.
In the case of a bigger particle, the thickness of EDL is negligibly small in the aqueous medium with the concentration of salt of 10^{-2} M and the f(Ka) is equal to 1.5. Based on this, Helmholtz-Smoluchowski equation (6) can be derived:

$$\mu_e = \frac{\varepsilon_0 \varepsilon_r \zeta}{\eta} \tag{6}$$

When the particles are in low salt dispersants 10^{-2} M and thickness of EDL can be even bigger than particle itself, the f(Ka) is equal to 1, the Hückel equation (7) can be obtained

$$\mu_e = \frac{2\varepsilon_0 \varepsilon_r \zeta}{3\eta} \tag{7}$$

The Helmholtz-Smoluchowski equation is popular for pharmaceutical preparations, i.e. nano-drug delivery, and the Hückel equation is mostly used in the ceramic industry [77].

2.8.3 Transmission electron microscopy

Visualization of nanomaterials by visible light microscopy is impossible, due to diffraction limitation. One of the very powerful techniques to describe the crystal structure, surface and chemical composition of materials whose characteristic dimensions are less than 100 nm in size is TEM. This method is providing direct, precise information about the size of particles, size distribution, shape and morphology [80], [81]. Using the HR-TEM (high-resolution TEM) method we can even characterise and control nanomaterials at an atomic-level of a structure [82].

Limitations of electron microscopy techniques are dry and solid samples. The thickness of the TEM sample which is usually less than 100 nm. Electrons must be able to penetrate the sample, but the sample should be resistant to high vacuum conditions. Therefore, a proper sample preparation is crucial for the microscopic image quality [82].

TEM was invented in 1931 by a German electrical engineer Max Knoll and German physicist Ernst Ruska. Magnification of the first TEM was just 17x. Three years after Marton and his colleagues in Brussels created the first images of nuclei by similarly built microscopes. These early TEMs used a series of the horizontal lenses in a column which differs from modern TEMs vertical arrangement of the lenses. First commercial TEM product was created in Siemens company (Germany) with a resolution of 10 nm and an accelerating voltage of 80 kV [80].

Construction of standard TEM follows the construction of a visible light microscope. In modern TEMs, electrons are emitted from the top of the column – electron gun assembly, afterwards electrons are accelerated to several hundreds of kV [81], [82]. TEM column is evacuated (the irradiation is stable under vacuum conditions) with a set of electromagnetic lenses and metal apertures which can focus electron beams from the source [80]. The focusing phenomenon is possible due to electron behaviour. Electrons, as negatively charged particles, are changing direction in the magnetic or electric field. This process leads to focusing electrons only with a well-defined energy range, which can pass through and these electrons interact with the sample in the column. The sample is on the TEM-grid (sample holder), and the sample position in the column is controlled by a mechanical arm [82]. After the sample surface interaction with the incident electron irradiation, the direct electrons, elastic or inelastic electrons and Bremsstrahlung X rays are the results of this interaction [72]. These transmitted electrons are refocused and subsequently magnified by a system of two lenses and displayed by phosphor screen (image conversion into the visible form). The significantly shorter wavelength of applied electrons (high acceleration voltage) enables the TEM's high resolution [82].

Observation techniques in TEM can be in bright-field or in the dark-field mode corresponding to transmitted or diffracted electrons. In the first case, the weakening of the transmitted direct electron scattering is used. According to the different density of the sample, the thicker areas and heavier atoms are displayed as darker areas. In the second mode, the transmitted electrons are not allowed to pass through the aperture, and the diffracted electrons are passing through and they form the dark-field images [82].

3 THE AIM OF WORK

The objective of the thesis is the optimisation of preparation and purification of fluorescent diamond nanoparticles stabilised with biocompatible polymers. The work will include the following particular tasks:

- Purification of fluorescent diamond nanoparticles
- Synthesis of biocompatible polymer shells on nanodiamonds
- Physico-chemical characterisation (light scattering, zeta potential, electron microscopy)
- Stability tests of the nanoparticles in an environment simulating physiological conditions

4 EXPERIMENTAL PART

4.1 Chemicals, standards and samples

4.1.1 Nanodiamonds

- Nanodiamonds 250 nm – Microdiamant, P9090
- Nanodiamonds 50 nm - Microdiamant, L11026-A
- Nanodiamonds 50 nm – Henan Huifeng Diamond Co. Ltd, 150630-402920

4.1.2 Chemicals used for polymerization

- Glycidol – Sigma-Aldrich, MKBZ8957V
- Glycidyl propargyl ether – TCI Chemicals, G0443

4.1.3 Chemicals used for CuAAC click reaction

- $CuSO_4 \cdot 5H_2O$ – PENTA, 210302
- Texas Red Azide – Click Chemistry Tools, 1111
- L-Ascorbic acid sodium salt, Alfa Aesar, 10193800
- Aminoguanidine hydrochloride – Sigma-Aldrich, MKBB3005
- HEPES – GENChem, 813JOT
- DMSO, HPLC grade– Acros Organics, A0391969
- Sulfonated BODIPY azide, BTTP, BTTPS, THPTA – synthesised in the laboratory

Other chemicals (p.a. quality) were purchased from commercial suppliers.

4.2 Used laboratory equipment

- Furnace Nabertherm P 330
- SIGMA Centrifuge 3-30 KS (SIGMA 13150 swinging rotor; SIGMA 12158-H)
- Ultrasonic Processor Cup Horn and Sonication Probe Cole Parmer
- Eppendorf Centrifuge 5430 R (rotor FA-45-24-11-HS)
- Magnetic Stirrer Heidolph MR Hei-Tec
- Lyophilizer LABCONCO
- CentriVap Concentrator LABCONCO
- Analytical Balance BOECO Germany BBC 22
- Balance BOECO Germany BBI 41
- Malvern Zetasizer Nano ZS
- Multimode Microplate Reader Tecan Spark®
- Transmission Electron Microscope JEOL JEM-1011
- Thermobalance Stanton-Redcroft TG750
- Nicolet 6700 - Thermo Scientific, USA + ATR prism - Pike Technologies, USA

4.3 Preparation and fraction separation of NDs

4.3.1 250 nm NDs

HPHT nanodiamonds (250 nm) were supplied by Microdiamant Switzerland. The NDs were oxidized by air oxygen (dry oxidation) in a tube furnace at 540 °C for 5 hours. Dry oxidation was followed by wet oxidation which was carried out in a HF:HNO_3 2:1 mixture (160 °C, 250 rpm, 2 days) in PTFE container on a magnetic stirrer. Scheme of NDs surface oxidation is in Figure 12. The NDs were separated from acids using centrifugation (4,000 g, 15 min), and washed with MiliQ water (2x50 ml), 1M NaOH (1x50 ml – neutralisation of inorganic acids), water (1x50 ml), 1M HCl (1x50 ml – protonation of surface carboxylic groups), MiliQ water (2x50 ml) (4,000 g, 10 min), MiliQ water (2x50 ml) (20,000 rcf, 20 min).

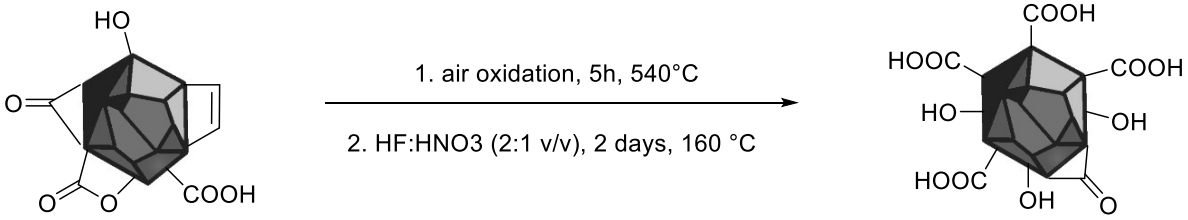

Figure 12 NDs surface oxidation (carboxylic group enrichment)

Washed oxidized NDs were separated based on their size. First, the pellets were resuspended in MiliQ water. The colloid solution after washing was 2x centrifuged (2,500 rcf, 20 min). After the second centrifugation, the supernatant was transferred to a 100 ml flask - fraction A. The pellets were pooled, resuspended in MiliQ water using cup horn sonication and then centrifuged (500 rcf, 30 min). The supernatant was removed and centrifuged again under the same conditions. Pellets were resuspended in MiliQ water as in the previous case. In total, centrifugation of supernatant was repeated 5 times. The supernatant after this series of centrifugations formed - fraction B. The pellets were pooled, 5 x centrifuged (500 rcf, 30 min), after centrifugation the supernatant was fraction C, the whole process was repeated one more time - forming fraction D. Resuspended pellets at the end of fractional centrifugation were labelled fraction E. The fraction A was additionally centrifuged (to isolate smaller particles), supernatant formed fraction As and pellets Ap.

4.3.2 50 nm NDs

HPHT NDs (50 nm) supplied by Henan Huifeng Diamond Co. Ltd and also Microdiamant Switzerland were oxidized by air oxygen in a tube furnace at 540 °C. After 3 hours half of NDs were removed and the rest of NDs, was oxidized for 3 more hours. Following mineral acid oxidation of both samples was carried out in HF:HNO_3 2:1 mixture and also in a mixture of H_2SO_4:HNO_3 9:1. Each NDs sample was treated with the 30 ml of the mixture containing hydrofluoric acid (160 °C, 250 rpm, 2 days) on a magnetic stirrer in PTFE container and also in the 40 ml mixture containing sulphuric acid (80 °C, 250 rpm) in a vial on a magnetic stirrer (Figure 13). The NDs were separated from acids using centrifugation (4,000 rcf, 30 min), and washed MiliQ water (2x50 ml), 1M NaOH (1x50 ml – neutralisation of inorganic acids), water (1x50 ml), 1M HCl (1x50 ml – protonation of surface carboxylic groups), MiliQ water (2x50 ml) (20,000 rcf, 20 min), MiliQ water (2x50 ml) (30,000 rcf, 20 min).

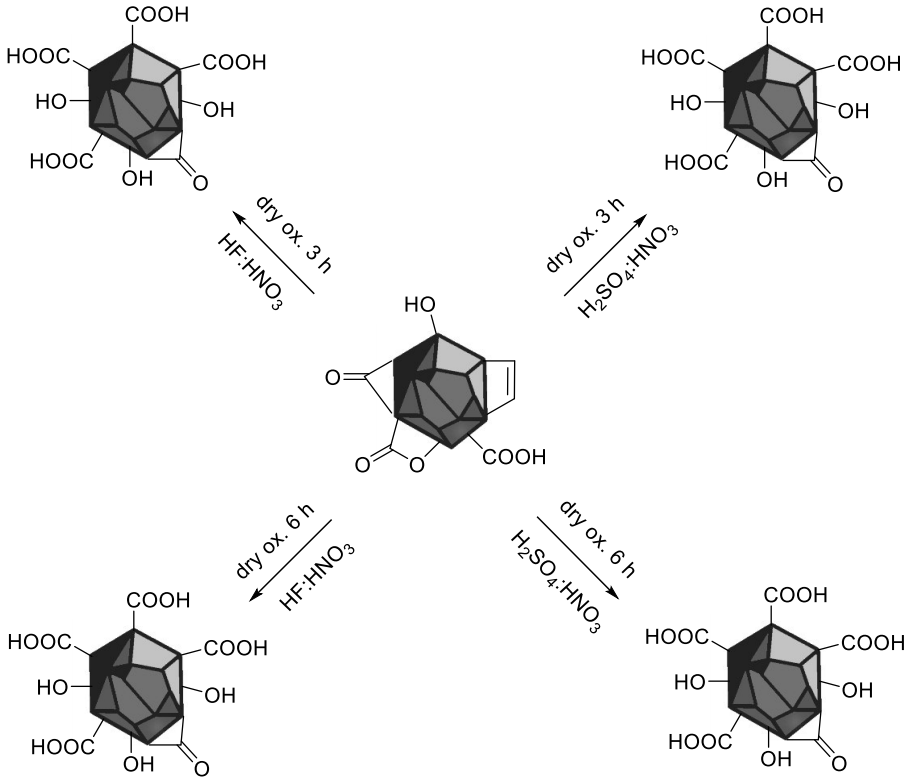

Figure 13 Scheme of different oxidation procedures of NDs from the production

4.4 Glycidol polymerization

4.4.1 Kinetics

Glycidol was freshly redistilled before every polymerisation under reduced pressure (~1 mbar, 50 °C) and mixed with the NDs (120 µl of glycidol per 1 mg NDs). NDs were dispersed in glycidol using cup horn sonication processor in pulse mode 2 s on, 2 s off, amplitude 100 % (1-4 h depending on type of ND; checked by DLS). The reaction (Figure 14) took place into a pressure tube in an oil bath on a magnetic stirrer (130 °C 200 rpm, 16 h). A volume equivalent to 1 mg of NDs was taken from the reaction mixture into Eppendorf microtube at following times: 0 h; 0.25 h; 0.5 h; 1 h; 2 h; 3 h; 6 h and 16 h. The reaction was quenched by MeOH addition. Then all the microtubes with the samples were washed (30,000 rcf, 15 min) with MeOH (2x1.5 ml) and MiliQ water (2x1.5 ml). Between the washing, each sample was sonicated for 2x10 s, amplitude 100 % at cup horn sonication processor.

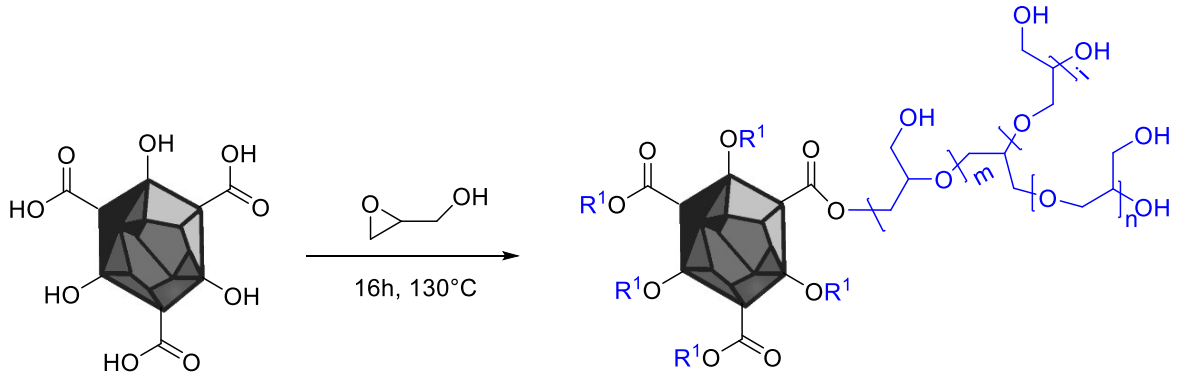

Figure 14 Glycidol polymerization scheme; R^1 corresponds to the polyglycerol layer (blue colour); both ethers and esters are formed during polymerization [44]

4.4.2 Propargyl termination

Glycidol was distilled under reduced pressure (~1 mbar, 50 °C). NDs were suspended in glycidol using cup horn sonication processor in pulse mode 2 s on, 2 s off, amplitude 100 % (1-4 h depending on type of ND; checked by DLS). The reaction (Figure 15) took place into a pressure tube in an oil bath on a magnetic stirrer (130 °C 200 rpm, 3 h). After 3 h, distilled glycidyl propargyl ether (~1 mbar, 60 °C) was added into reaction mixture. NDs with different glycidol:glycidyl propargyl ether molar ratios were prepared – 90:10; 80:20; 70:30 (vol: 102.1+18.4; 86.0+34.8;71.4+49.4 µl per 1 mg of NDs). The reaction continued at the same conditions overnight. The NDs were washed (30,000 rcf, 15 min) with MeOH (2x1.5 ml per 1 mg of NDs) and MiliQ water (2x1.5 ml per 1 mg of NDs). Between the washing, each sample was sonicated for 2x10 s, amplitude 100 % at cup horn sonication processor.

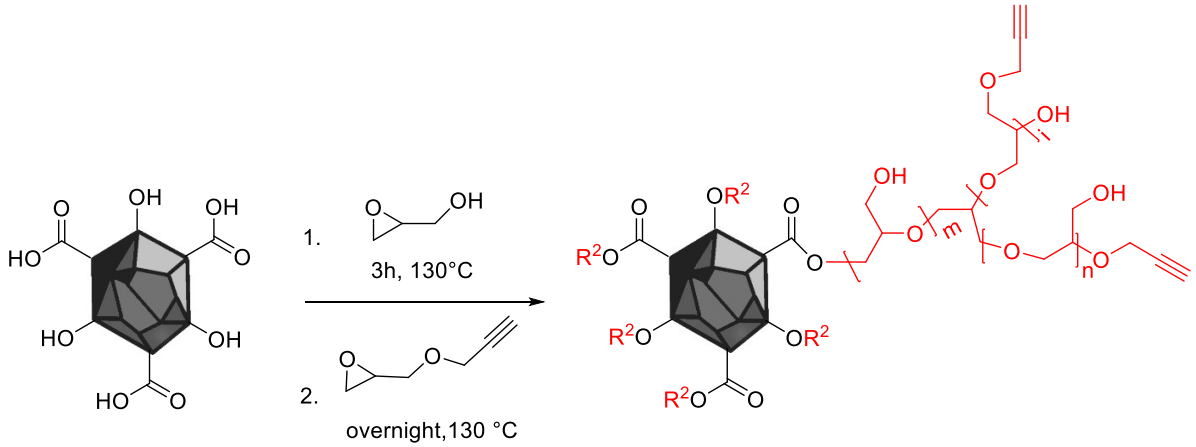

Figure 15 Polyglycerol coating with terminal alkyne groups; R^2 corresponds to the propargyl terminated polyglycerol layer (red colour); both ethers and esters are formed during polymerization [44]

4.5 CuAAC click

4.5.1 Stock solutions

All the solutions needed for CuAAC click reaction were prepared with stock concentration (c_{stock}) according to the following Table 1. The aminoguanidine, L-sodium ascorbate, organic dyes – Figure 16 (BODIPY azide and Texas Red PEG_3 azide), $CuSO_4 \cdot 5H_2O$ and HEPES buffer solutions were prepared in MiliQ water. Ligands (THPTA, BTTP, BTTPS) were dissolved in DMSO. Cu(II) salt + ligand solutions were pre-mixed before reaction (volume ratio of stock solutions 1:1). The stock solutions used in CuAAC reaction except L-sodium ascorbate are long-term stable. The L-sodium ascorbate was freshly prepared before each reaction.

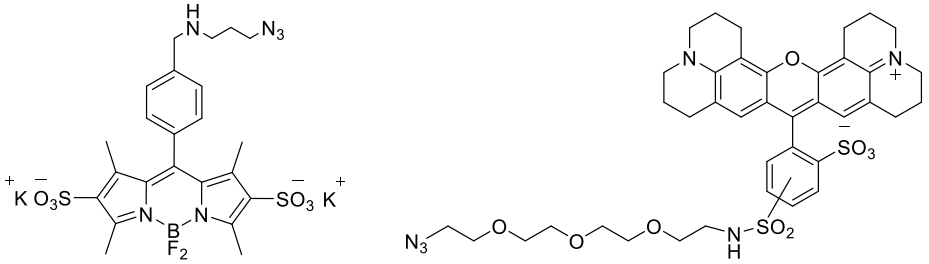

Figure 16 Sulfonated BODIPY azide (left). Texas Red PEG_3 azide (right)

Table 1 Reagents for the CuAAC click reactions

Reactant	M_w (g·mol^{-1})	c_{stock} (mM)	V_{stock} (ml)
Bodipy azide/Texas Red PEG_3 azide	594.14/ 625.151	20	0.2
CuSO4·5H2O	249.68	50	1.0
BTTP/ BTTPS/ THPTA	430.56/ 494.62/ 530.63	100	0.5
Amioguanidine hydrochloride	110.55	100	1.0
L- Sodium ascorbate	198.11	100	1.0
HEPES pH 7	238.30	250	10

4.5.2 Optimisation of click reaction

50 µl of ND-PG-alk20 solution (0.25 mg NDs) was pipetted into Eppendorf microtube (1.5 ml) and then diluted by the same volume of DMSO (reaction was carried out in ~50 % DMSO). Then the reagents were combined in the following order: ND-alkyne, dye-azide, premixed solution of $CuSO_4$ and ligand, aminoguanidine, HEPES and L-Sodium ascorbate was added as the last reagent (reaction initiation). Reactants ratios and final concentrations are shown in Table 2. The tube was closed and mixed by a vortex. The reaction was allowed to proceed for 1.5 h at RT. After the reaction, NDs were washed by 50 % DMSO (5x1ml).

Table 2 Example of click – molar ratios and final concentration of reactant stock solutions

Reactant	1		2		3		4	
	molar ratio	c_{final} (mM)	molar ratio	c_{final} (mM)	molar ratio	c_{final} (mM)	molar ratio	c_{final} (mM)
0.25 mg ND-PG-alk20 (~50% DMSO)	1	0.06	1	0.06	1	0.06	1	0.05
Sulfonated BODIPY N_3 Texas Red PEG_3 N_3 D-mannose PEG_3 N_3	5	0.30	5	0.30	5	0.28	5	0.25
$CuSO_4·5H_2O$	0.2	0.01	1	0.06	5	0.28	25	1.27
THPTA/BTTP/ BTTPS	0.4		2		10		50	
Aminoguanidine hydrochloride	2	0.02	10	0.12	30	0.57	50	2.55
L- Sodium ascorbate	2	0.12	10	0.59	30	1.70	50	2.55
HEPES pH 7		0.12		0.59		1.70		2.55

4.5.3 D-mannosylation

500 µl of 3FND-PG-alk water solution (10 mg of the FNDs) was pipetted into Eppendorf microtube (2 ml). Then, the reagents were combined in the following order: ND-alkyne, D- mannose PEG_3 azide, premixed solution of $CuSO_4$ and BTTP, aminoguanidine, HEPES and L- sodium ascorbate was added as the last reagent (reaction initiation). Reactants ratio corresponds to the 4th column in Table 2. The tube was closed and mixed by the vortex. The reaction (Figure 17) was allowed to proceed for 1.5 h at RT. After the reaction, NDs were washed by MiliQ water (5x5 ml).

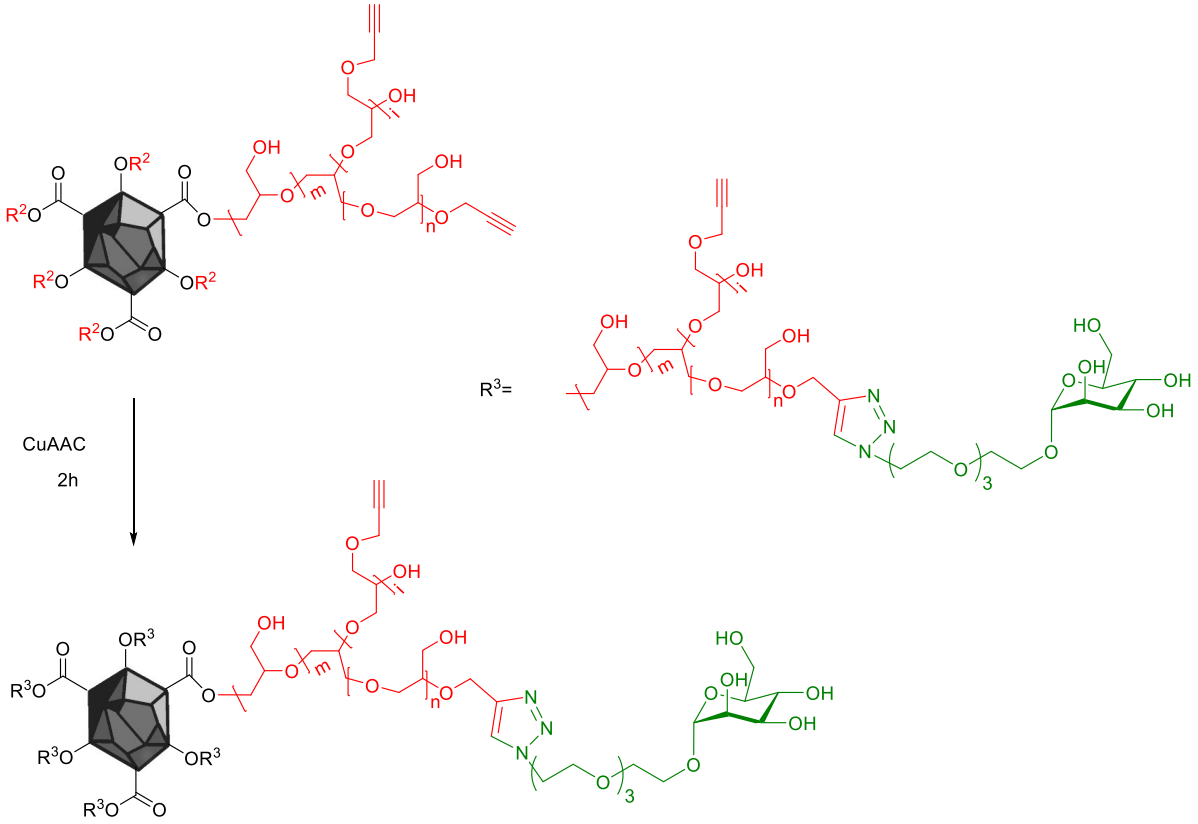

Figure 17 CuAAC click reaction scheme (D-mannosylation of FND-PG-alk30)

4.6 Dynamic light scattering

4.6.1 Size distribution

The nanodiamonds size was measured in the disposable transparent cuvette at RT in MiliQ water, 1xPBS and 10xPBS. The sample concentration was ca 0.05 mg/ml, a total volume of 1 ml.

4.6.2 Aggregation kinetics in FBS

Aggregation of NDs was investigated in FBS medium at 37 °C (viscosity 0.861 cP) [83]. The NDs concentration in FBS was 0.5 mg/ml; the sample volume was 100 µl in total (dilution of 100 % FBS by NDs ~ 5 % vol.). The particle size was measured in 10 following measurements over 30 minutes in Quartz cuvette ZEN2112.

4.7 Zeta potential

The zeta potential of NDs was measured using dip cell for zeta potential in MiliQ water at RT. The sample concentration was ca 0.05 mg/ml, total volume of 1 ml.

4.8 Transmission electron microscopy

4.8.1 Sample preparation

For the TEM sample preparation, the carbon-coated copper grids (Pyser) were used. Before the sample application, the grids were placed into a UV-ozone chamber for 15 mins. Then the grid was placed on the poly(ethyleneimine) solution droplet (Mw = 2.5 kDa, 0.1 mg/ml). After two minutes was the solution dried up by tissue. Then, the grid was placed on the sample solution droplet (0.1 mg/ml) and after 2 min was also removed by tissue [84].

Tungstic acid (2 wt%, pH 7) was used for staining of polymers. The grid was first placed on the sample solution droplet (0.1 mg/ml). After 2 min the grid was placed (without drying by tissue) on the water droplet (2x1 min) and finally on the tungstic acid solution (2x1 min).

TEM images were recorded by Helena Raabová, IOCB, Prague.

4.8.2 Image analysis

Particle size distributions were analysed using ImageJ software. Each picture was processed in the same way. At first third-order fitting was applied to remove uneven illumination, then Gaussian blur (2 pixels) filter was used to remove background noise. The threshold was set to create a binary image. Connections of nanodiamonds caused by thresholding were divided manually with 2-pixel width lines according to original images. The number of connected particles was small, so there is a negligible effect of this procedure on the data. In total, 250-300 particles per sample were analysed.

Total areas of the particles (nm^2) were obtained after analysis because nanodiamonds have an irregular shape. Due to this, we used the equivalent circular diameter for size expression. Equivalent circular diameter is described by the following equation (8)

$$d_{eq} = \sqrt{\frac{4S}{\pi}} \tag{8}$$

Equivalent diameter is the diameter of a circular particle with the same area as the area of the nanodiamond [84].

4.9 Absorbance and fluorescence measurements

4.9.1 Sample preparation

Absorbance scans were measured by Multimode Microplate Reader ranging between 300 nm and 700 nm. The fluorescence scans were also measured. The wavelength of collected excitation was from 400 nm to 600 nm. The sample concentration was 0.17 mg/ml.

4.9.2 Data fitting

The raw absorbance data were processed using MestReNova BETA testing software for UV-VIS data analysis. The Asymmetric Least Square (ALS) baseline correction was used for data fitting – Rayleigh scattering elimination. This baseline correction is easily tuned just by selecting a few factors without selecting any anchor points. The fitted data was plotted and integrated using Origin 8 Pro software.

4.10 Thermogravimetric analysis

Thermogravimetric analysis was carried out using thermobalances. The samples (1,7-2,3 mg) were placed on a platinum pan and heated up to 900 °C at a rate of 20 °C/min under air purge (20 ml/min).

The analysis was performed at Laboratory of Thermo-Gravimetric Analysis, UCT, Prague.

4.11 Fourier-transform infrared spectroscopy

FTIR spectra were recorded on a spectrometer using standard MIR source, KBr beamsplitter, and DTGS detector which was purged with nitrogen. KBr pellet (diameter 4 mm) contains 0,9 mg of a sample and approx. 150 mg of KBr. Spectrometer operated in transmission mode: 128 scans, 2 cm^{-1} spectral resolution, Happ-Genzel apodization function. Recorded spectra were normalized.

ATR-FTIR mode of measurements was measured using a single-reflection diamond horizontal ATR prism. Measurement setup was: 256 scans, 4 cm^{-1} spectral resolution, Happ-Genzel apodization function. For the ATR-FTIR spectra, the spectrum of water vapour was subtracted.

FTIR analyzes were done by Dr. Lucie Bednárová, IOCB, Prague.

5 RESULTS AND DISCUSSION

This thesis is focused on preparation and characterisation of FNDs coated with a biocompatible polyglycerol layer, functionalized with terminal propargyl group used from subsequent D-mannose attachment for specific sentinel lymph node(s) targeting *via* macrophages. Prepared NDs are characterized mainly according to their size and stability, using physicochemical methods for standard nanoparticle characterization, such as DLS, TEM and zeta potential (ZP). Surface and size characterization of NDs combined with their stability in biological environment is essential for their further biomedical applications.

5.1 Oxidation of NDs

5.1.1 250 nm

2.05 g HPHT NDs (MicroDiamant) were subjected to the aerobic oxidation (dry oxidation) in the furnace over 5 h at 540 °C. After the dry oxidation, ND's weight was 1.76 g (yield 85.9 %). Weight loss can be caused by the decomposition of graphitic impurities of the ND surface at high temperature. NDs were oxidized after dry oxidation by inorganic mineral acid mixture, 1.70 g (yield 82.9 %) NDs was obtained after this procedure. NDs were purified from acids several times in MiliQ water, 1M NaOH and 1M HCl. NaOH solution was used for mineral acid neutralisation, and HCl solution was used to protonate back carboxylic groups on the NDs surface. After the purification procedure, 1.56 g (yield 76.1 %) of NDs were obtained and were further separated by size.

5.1.2 50 nm

Oxidation of small NDs was carried out at several different conditions, both for dry and wet oxidation. This experiment was performed to study the effect of different oxidation conditions on ND's surface chemistry and further modification.

5,00 g HPHT NDs (Henan Huifeng Diamond) were also subjected to both dry and wet oxidation. Dry oxidation was performed at 540 °C for 3 h and 6 h, respectively. During the wet oxidation, different acid mixtures were used. 1.92 g NDs was removed from the furnace after 3 h,2.42 g of NDs was oxidized for 6 h. The final amount of NDs after the dry oxidation was 4.34 g (yield 86.8 %). Each oxidized sample was further halved and oxidized using two different protocols for wet oxidation (either $HF:HNO_3$ 2:1 (v/v), 160 °C and $H_2SO_4:HNO_3$ 9:1 (v/v), 80 °C). All the samples were further purified from acids using same procedure as described above. The total amount purification and subsequent lyophilization was 3.43 g (yield 68.6 %). Yields of four differently oxidized NDs samples are shown in the Table 3.

2.01 g HPHT NDs (MicroDiamant) were also subjected to both dry and wet oxidation. Dry oxidation was performed 3 h and 6 h, respectively. During the wet oxidation, different acid mixtures were used again. Amount of 0.925 g NDs was removed from the furnace after 3 h and 0.636 g of NDs was oxidized for 6 h. The total amount of NDs after the dry oxidation was 1.76 g (yield 87.6 %). Each oxidized sample was further halved and oxidized using two different protocols for wet oxidation (either $HF:HNO_3$ 2: 1 (v/v), 160 °C and $H_2SO_4:HNO_3$ 9:1 (v/v), 80 °C). All the samples were further purified from acids using same procedure as described above. The total amount purification and lyophilization was 1.43 g (yield 71.1 %).

The highest yield of NDs was obtained in the case of oxidation of bigger NDs (250 nm) in comparison with smaller ones (50 nm). This result was expected, because the same amount of the smaller particles has larger surface area in comparison with the bigger ones. Due to this fact, weight loss caused by oxidation is more significant than in the case of the smaller NDs. NDs material loss caused by oxidation can be up to 30 % and some material can be lost by handling (usually 1-2 %). Therefore our obtained values of NDs practical yields are in standard range (from 70 % to 90 %).

Oxidized NDs were characterized by zeta potential to obtain quick NDs stability description. No significant differences were observed between obtained ZP values. However, better colloidal stability according to faster sonication before polymerization reaction was observed in the case of samples which were oxidized longer and where the hydrofluoric acid mixture was used. This treatment was recognized as the best and therefore was used for NDs surface oxidation.

Table 3 Yields of NDs after oxidation treatment at different conditions

Time of dry oxidation (h)	**Wet oxidation mineral acid mixture type**	**Micro Diamant**	**Henan Huifeng Diamond**
		yield (%)	
3	H_2SO_4+HNO_3	78.9	74.7
3	HF+HNO_3	83.3	81.5
6	H_2SO_4+HNO_3	84.7	90.4
6	HF+HNO_3	77.6	88.5

5.2 Size separation

Purified 250 nm NDs were separated by size, because of their wide size distribution from the production. Five fractions were obtained after the fraction centrifugation, the total mass of the NDs after lyophilisation was 1.03 g (yield 50 %). Fraction A was later split using centrifugation into two (fraction As – supernatant and Ap – resuspended pellets) to obtain the smallest NDs with narrow distribution of size. The efficiency of the NDs separation by size was examined using DLS measurement and more precise TEM image analysis.

5.2.1 DLS

The size distribution of each NDs fraction after the oxidation process and subsequent purification was measured by DLS. Results of the measurement are shown in Figure 18. Masses of individual fractions with hydrodynamic diameters and polydispersity indexes (PDI) are shown in Table 4. According to the DLS results, we can see that the size distribution of individual fractions is shifted to the bigger hydrodynamic diameter values (Figure 18). Zeta potential of individual NDs fractions was measured. Differences between ZP values of fractions are included in the range of the instrument limitation. Negative ZP values are observed because of oxidized NDs surface containing deprotonizable carboxylic groups.

Table 4 Practical yields and DLS results of NDs fractions

fraction	m (mg)	d (nm)	PDI	ZP
A	110.26	106	0.089	-22
B	490.80	145	0.081	-23
C	63.20	162	0.134	-17
D	34.85	180	0.152	-20
E	610.10	205	0.116	-24

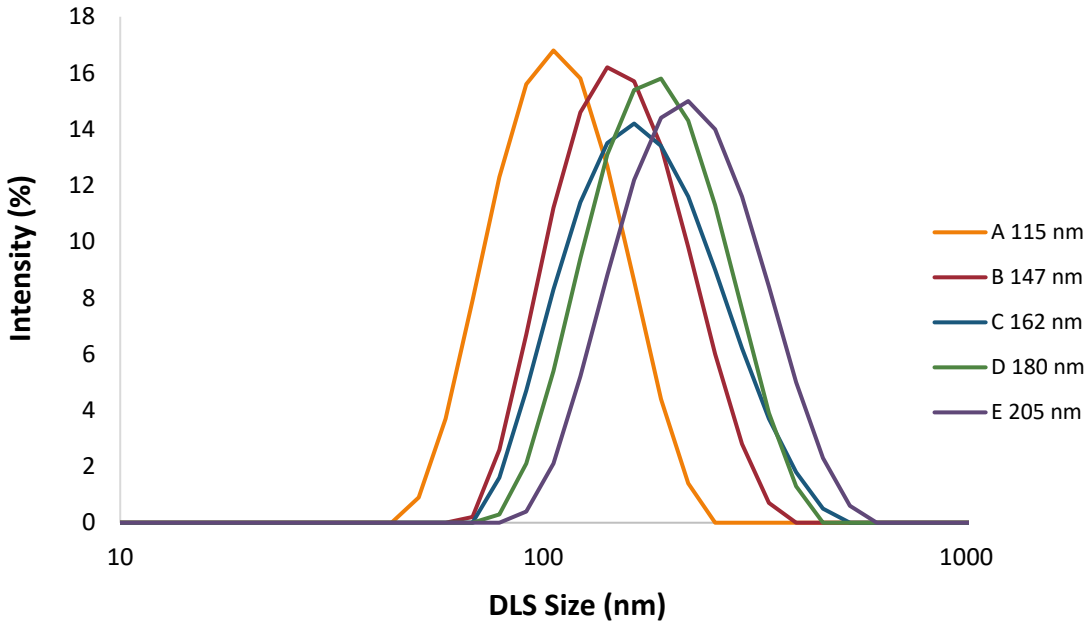

Figure 18 Size distribution of NDs fractions after the size separation process; the values correspond to the average hydrodynamic diameter

5.2.2 TEM

Direct information about NDs size can be obtained using TEM. TEM bright-field images of all fractions are shown in Figure 19 (resolution 40,000x). According to the images, we can see the irregular shape of NDs and increasing NDs size from the fraction As to the fraction E. This trend was further confirmed by image analysis.

Analysis of particle size distribution from TEM images was performed using ImageJ software. The binary image was created during the image analysis from the original bright-field image (Figure 20). Values of the NDs area were obtained for individual particle. The particle size was described by the circular equivalent diameter, which was calculated for each particle from corresponding NDs areas. Volumes were also calculated for each particle, as if they were spheres, using circular equivalent diameter. Therefore, two types of histogram plots were created. One histogram type shows number-weighted distribution (Figure 21), where the weighting of each particle is the same regardless of its mass. The second type of histograms shows volume-weighted distribution (Figure 21).

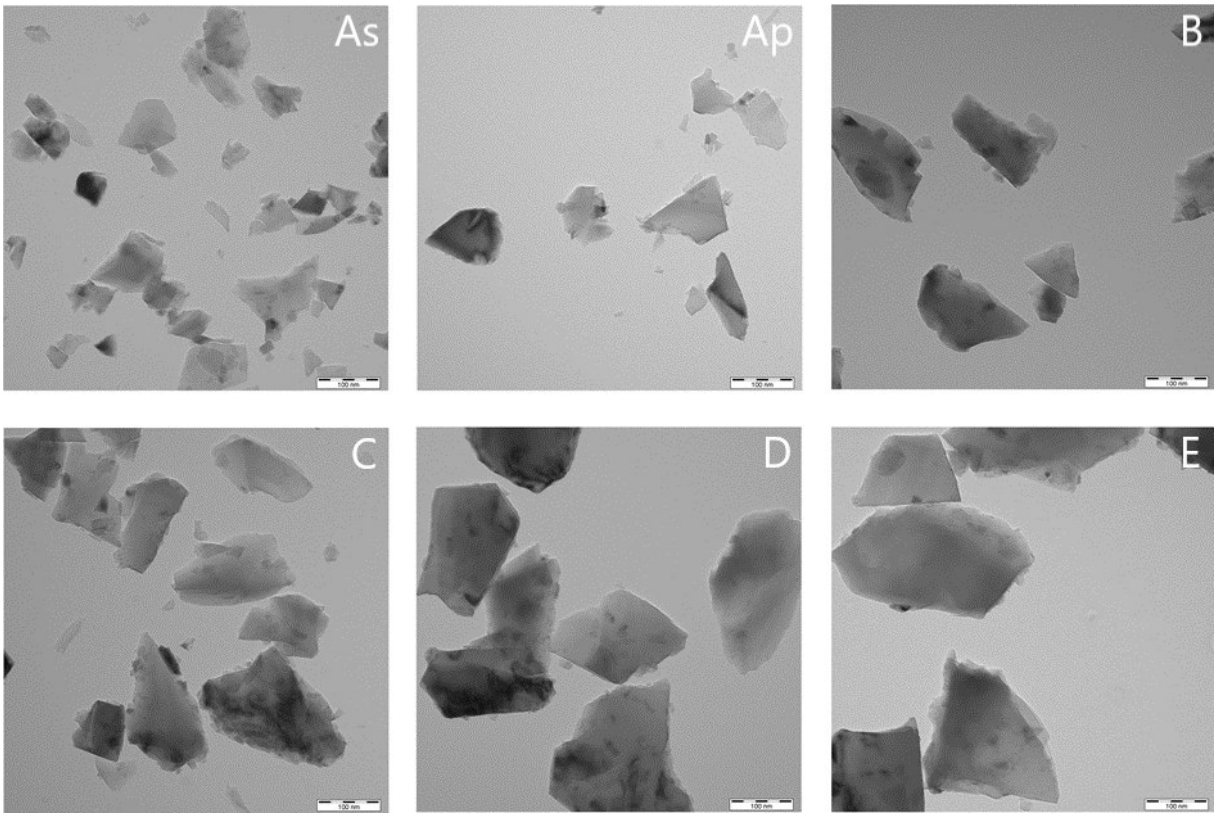

Figure 19 TEM images of NDs fractions after size separation (resolution 40,000 x)

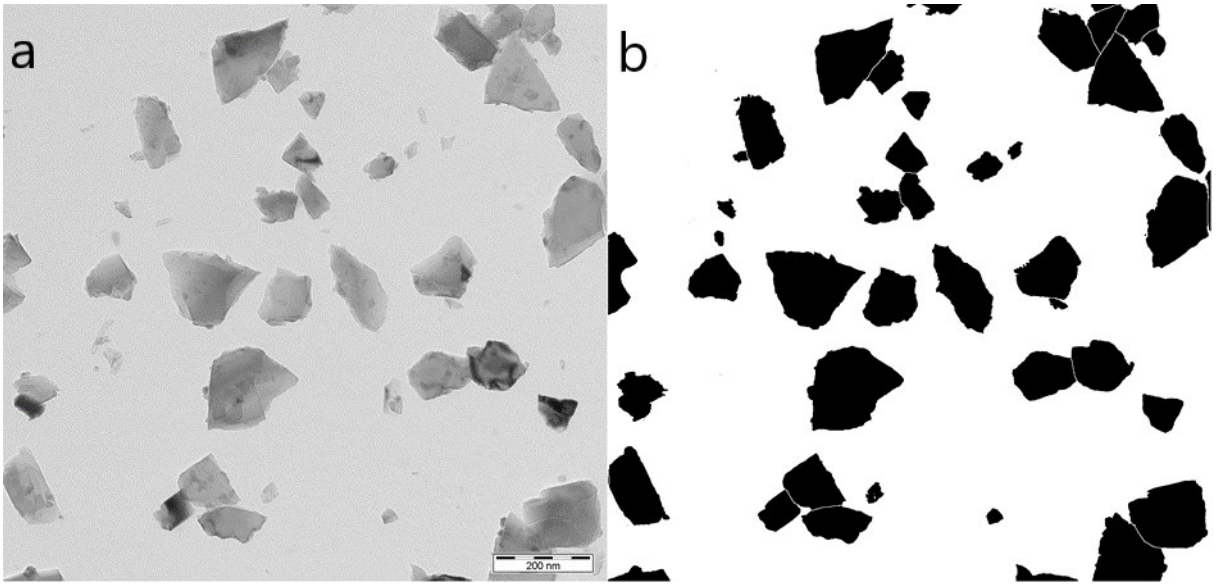

Figure 20 TEM image analysis procedure, (a) original bright-field image, (b) processed binary image; resolution 10,000 x

Number-weighted distribution histogram of fraction As (Figure 21) shows non-symmetric bimodal character. We identified two dominant size intervals, first ranging between 15 and 30 nm and the second ranging between 75 nm and 90 nm. The number-weighted histogram of fraction C (Figure 21) shows the biggest occurrence of NDs size 0-15 nm. Then intervals 15-30 and 90-105 nm have the same relative frequency (the second highest). In the case of number-weighed distribution of NDs fraction E (Figure 21), the significant maximum is in the interval 0-15 nm.

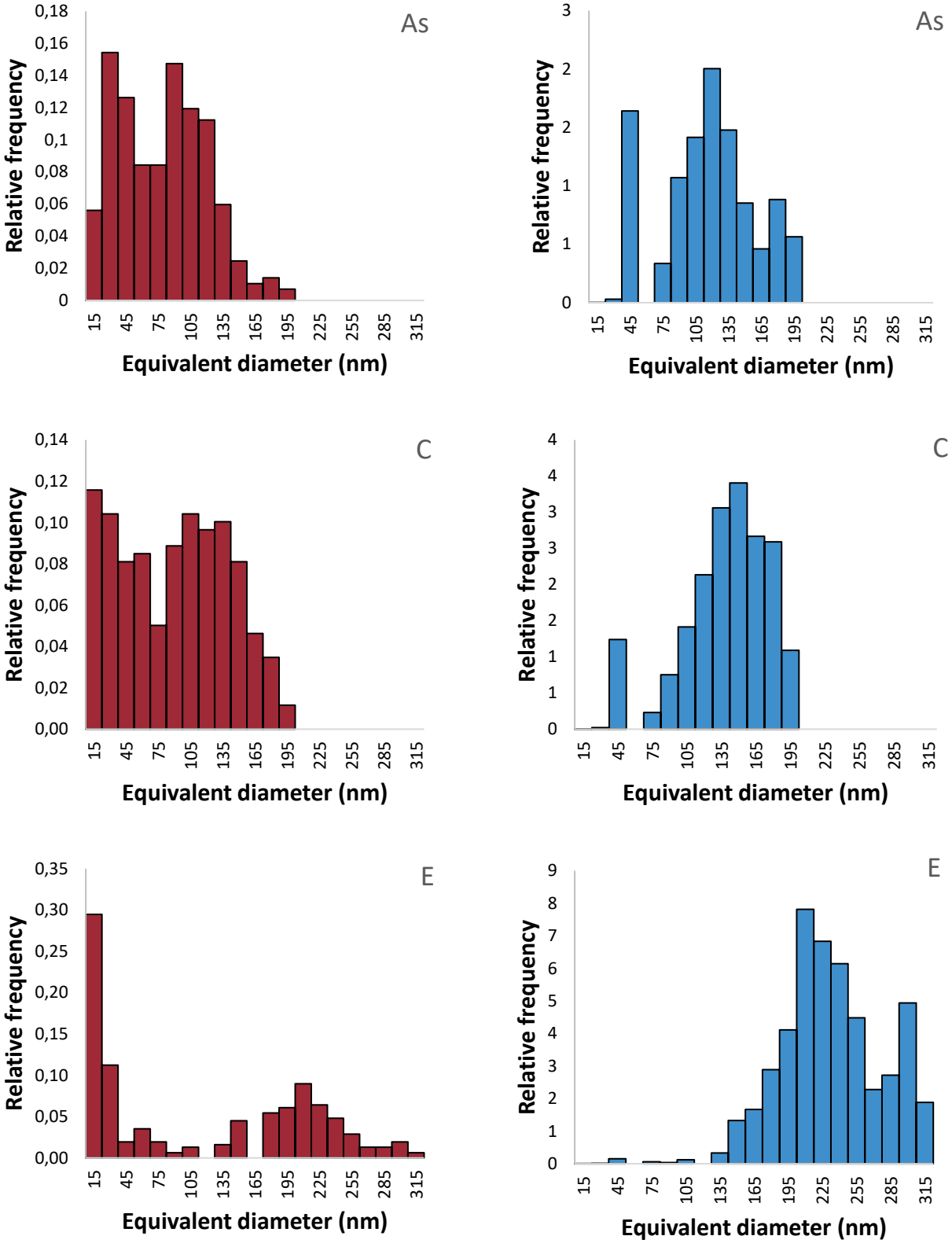

Figure 21 TEM histograms; number-weighted size distribution (red); volume-weighed size distribution (blue) for fractions As, C and E

Volume-weighted histogram of NDs fraction As (Figure 21) also shows non-symmetric bimodal character; first local maximum is at 30-45 nm and the second between 105 and 120 nm. The most frequently present particles according to the volume-weighted distribution of fraction C (Figure 21) are in the interval 135-150 nm. The maximum of last volume-weighed histogram corresponds to fraction E is in the interval 195-210 nm.

Smaller particles occurre indeed less in the all volume-weighted histograms in comparison with the number-weighted ones. In volume-weighted histograms, we can also see the shift of dominant intervals to the bigger sizes – to the right what correspond with the observation of individual fractions by TEM (Figure 20) and DLS measurement (Figure 18).

Size separation of 250 nm NDs is quite difficult procedure because during the centrifugation two processes/effects are potentially occurring. Larger NDs pulling-down the smaller NDs during sedimentation and usually smaller NDs are also sticking to the larger ones. To confirm if the size separation was efficient, DLS measurement and TEM observation were used. DLS size results showed that hydrodynamic diameter increases from fraction A to fraction E which corresponds with our expectation. The same trend is observed from the TEM images. However, results of TEM image analysis according to the number weighed distributions show, surprisingly, relatively high number of small particles with size smaller than 30 nm. These particles are present also in the fraction E, where the relative frequency is most significant in comparison with fraction A and C and they are not sticking to larger NDs. The values of DLS sizes of individual fractions correspond with the most frequently occurring size intervals in volume weighted histograms from TEM.

5.3 Glycidol polymerization

Nanodiamonds, both fluorescent and non-fluorescent, were coated using glycidol or glycidol in combination with glycidyl propargyl ether. These monomers were polymerized with hydroxylic and carboxylic groups present on oxidized NDs surface. All the mentioned polymerization were repeated at least twice with similar yields higher than 90 %.

Preparation of ND-PG-OH: 11.56 mg of NDs (fraction E, 205 nm) were sonicated with 1.39 ml of freshly distilled glycidol (M1) in microtube (2 ml) and the polymerization reaction was allowed to proceed at 130 °C overnight. Reaction was quenched by MeOH addition and prepared ND-PG-OH were washed by MeOH (2x) and water (2x). A water solution of ND-PG-OH was obtained, after washing, with concentration 2.5 mg/ml, volume 3.8 ml.

Preparation of ND-PG-alk was similar to ND-PG-OH, but also second monomer (M2), glycidyl propargyl ether, was added after 3 h. Approx. 15 mg of NDs (fraction E, 205 nm) were polymerized. The same procedure was used for modification of FND-PG-OH. All ND's sample weights with different volumes of monomers used for the polymerization (M1 corresponds to glycidol; M2 glycidyl propargyl ether) are shown in the Table 5.

Table 5 Amounts of NDs and monomers used for polymerization

sample	m (NDs) (mg)	molar ratio M1:M2	V (M1) (µl)	V (M2) (µl)
ND-PG-alk10	14.75	90:10	1,500	270
ND-PG-alk20	15.52	80:20	1,334	539
ND-PG-alk30	15.56	70:30	1,111	769
FND-PG-alk30	10.56	70:30	736	509

5.3.1 TEM

Tungstic acid (TA) is a heavy metal anionic compound commonly used for negative staining in TEM [85]. Staining of NDs samples (50 nm) was used for possible visualization of the polyglycerol layer in TEM. Bright-field TEM images of NDs and ND-PG both stained and non-stained were obtained, and they are shown in Figure 22. According to the images, we can see that polymerized NDs (Figure 22-1b; 2b) are more spread in comparison with non-modified NDs - TEM artefact (Figure 22-1a; 2a). The TEM images of stained and non-stained NDs without PG layer are similar. Also, the image for non-stained polymerized NDs shows similar contrast. However, it should be noted that the stained modified NDs are brighter than their close surrounding (PG layer). Based on the fact, that in bright field imaging, heavier atoms are displayed darker, the darker areas around the NDs correspond to the tungstic acid (different atomic weight of carbon and tungsten). This observation can be a result of non-specific interactions between the polymer layer and tungstic acid. Therefore, indirect evidence of the PG layer was obtained. Presence of the PG layer was further investigated using DLS and finally confirmed by TGA and stability tests.

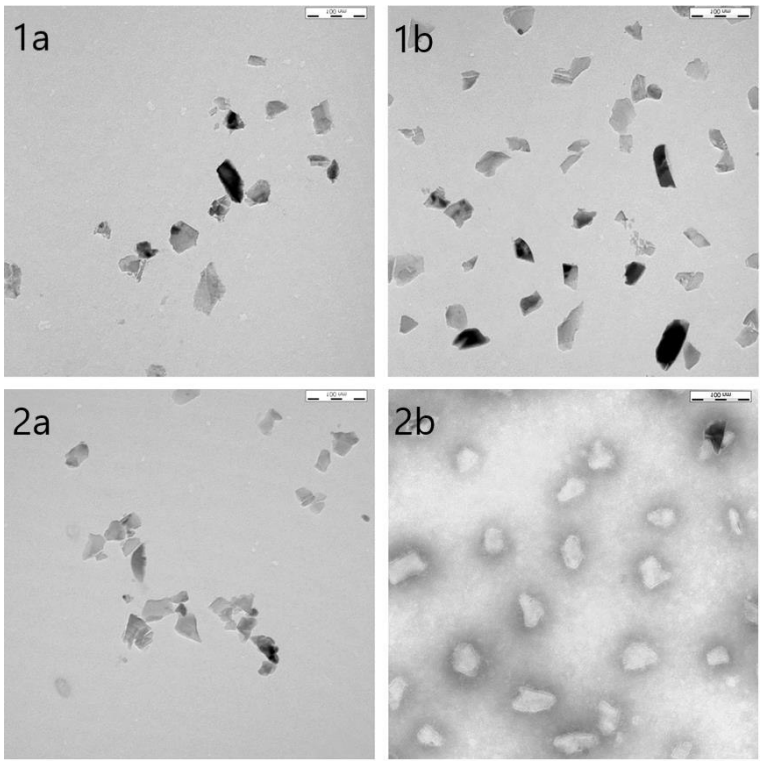

Figure 22 TEM image of NDs (50 nm resolution 10,000x) (a) before polymerisation; (b) after polymerisation; (1) without tungstic acid staining; (2) with tungstic acid staining

5.3.2 DLS - kinetics

The smallest fraction of NDs (fraction As) was used for kinetics studies. This fraction was selected for elimination of measurement inaccuracy (due to expected higher increase in layer thickness during the reaction in comparison to the ND. Kinetics measurements were performed in triplicate; all the hydrodynamic diameter values are plotted as the function of time (Figure 23). The hydrodynamic diameter of NDs increased from 115 nm to 147 nm, during the polymerization (20 h). The results of this measurement are not easily reproducible. According to this study, the time 3 h after reaction beginning, was chosen as the most suitable time for the second monomer addition into the reaction, in order to prepare stable ND-PG containing alkyne group and the PG layer as thin as possible. The polyglycerol layer presence was further investigated by TEM, thermogravimetric analysis and during stability tests in PBS and FBS.

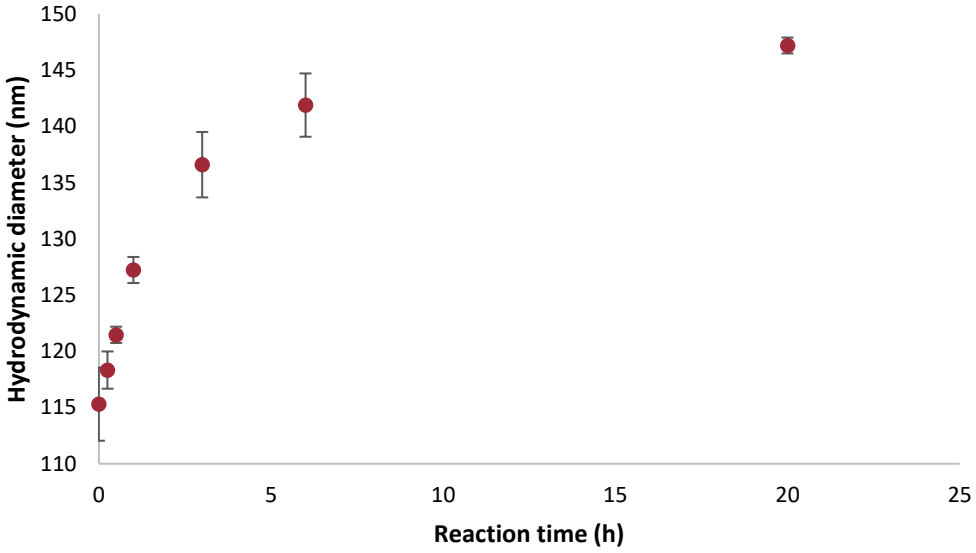

Figure 23 Kinetic study of PG layer growth on ND surface (fraction As); error bars show standard deviation of 3 size measurements

5.3.3 TGA

The thermal decomposition of ND-PG with different thickness of layer was studied by TGA and compared with non-modified NDs (carboxyl-enriched). The samples (approx. 2 mg) were heated up to 900 °C at a constant rate. The mass change in percentage is plotted against temperature (known as TGA curve) which is the typical result of this analysis, and it is shown in (Figure 24).

TG curve corresponding to NDs sample shows the typical single-stage decomposition having T_i (starting decomposition temperature) and T_f (final temperature), which is the lowest temperature of a mass change. The first portion of the curve is horizontal, ranging from 20 °C to 555 °C and indicate no weight loss of the sample. Decomposition of ND starts at the temperature 555 °C and last until 821 °C (weight loss 99.84 %). At the temperatures higher than 821 °C is the TG curve also horizontal without significant change in weight.

The TG curves of ND-PG show multistage decomposition according to various processes that occurred during the sample heating. The first stage of these curves is also horizontal (without serious weight change), interval 20-247 °C corresponds to TG curve of ND-PG-OH

(molar ratio of glycidyl ether: glycidyl propargyl ether equals to 100:00) and the range 20-220 °C for the case of ND- PG-alk30 (molar ratio of glycidyl ether: glycidyl propargyl ether equals to 70:30). TG curve of ND-PG-alk30 shows the PG decomposition occurred in the interval 247-372 °C (weight loss 3.38 %). At the stage 609-780 °C (weight loss 95.05 %) NDs decomposition occurs. TG curve of ND-PG-alk30 shows PG decomposition at the temperature values ranging between 220 and 445 °C (weight loss 7.78 %) and nanodiamond decomposition from 590 to 774 °C (weight loss 88.65 %). In the case of ND-PG-OH is the percentual weight loss of PG approx. twice as big as the weight loss of ND-PG-alk30. This mass difference of PG coating corresponds to the fact, that propargyl containing monomer addition terminates the PG layer growth. Only thin PG layer is formed over first 3 h (before propargyl monomer addition) in comparison with 20 h long glycidol polymeration.

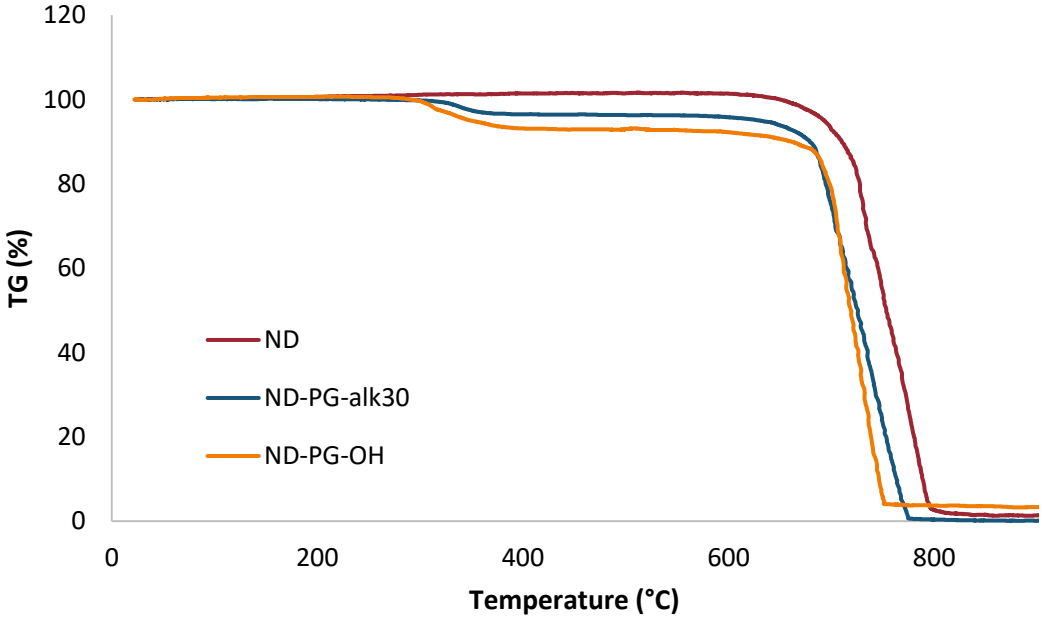

Figure 24 Thermogravimetric curves of oxidised NDs and NDs with a polyglycerol layer of different thickness

Our expectation was, that NDs size during glycidol polymerization increases. To confirm this hypothesis DLS size measurement, TEM observation and thermogravimetry were employed. Increase of hydrodynamic diameter around 30 nm was observed over 20 h during kinetics study. Indirect evidence of present polyglycidol layer after negative staining was obtained according to TEM images. Therefore, it can be stated that glycidol polymerization was successful and NDs are covered with hyberbranched polyglycerol layer. Presence of polyglycerol layer on NDs surface was further comfirmed during stability studies. Polymer layer is thicker in the case of ND-PG-OH particles in comparison with ND-PG-alk30, because polymerization is not terminated by alkyne addition (decrease of branching possibilities). Formed polyglycerol layer can form almost 8 % of ND-PG-OH mass according to the TGA results. According to the literature, the layer thickness was calculated as difference between core size determined by STEM (Scanning transmission electron microscopy), and hydrodynamic size, which is approx. 7 nm [49]. In another case, ND-PG were prepared with the STEM core size around 16 ± 12 nm and hydrodynamic size 37 ± 25 nm [87].

5.4 CuAAC click optimisation

Fluorescence dyes containing azide group (Sulfonate BODIPY azide and Texas Red azide) were reacted with the propargyl functionalized NDs surface to determine CuAAC click reaction efficiency using fluorescence and absorbance measurements. Data obtained during the reaction optimisation are important for further D-mannosylation of fluorescent nanodiamonds. Effect of various factors influencing the amount of attached dye on ND-PG-alk surface was investigated, such as type of solvent for the click reaction, amount of propargyl-containing monomer used for glycidol polymerization, type of ligand and concentration of catalyst. For each click reaction during optimisation 0.25 mg of NDs were used in 100 µl DMSO: water 1:1 v/v mixture, other reactants were calculated according to reactant ratios showed in (Table 2).

First, different solvents (water, DMSO, MeOH and dioxane) were used as potential environments for the reaction of ND-PG-alk20 (molar ratio of glycidyl ether: glycidyl propargyl ether equals to 80:20) with sulfonated BODIPY azide. Dioxane causes fast precipitation of ND-PG-alk20. Precipitation also occurred in the MeOH. Finally, as the most suitable solvent chosen for the reactions was DMSO:water mixture with ratio 1:1 v/v, because of the best-observed solubility of all reaction components.

5.4.1 Fluorescence

During the click reaction optimization, only 0.25 mg alkyne containing NDs reacted with fluorescent dyes. Based on low concentration of dye as well as expected low substitution of propargyl groups on the ND surface, fluorescence spectroscopy, as one of the most sensitive instrumental methods, was used for CuAAC reaction efficiency examination.

However. these results of fluorescence measurement were not used for CuAAC efficiency investigation and quantification of fluorescent dye attachment, because of the observed fluorescence quenching caused by high concentration and close proximity on the surface. Because of this finding, absorbance measurement was employed to determine the click efficiency. Excitation spectra of sulfonated BODIPY azide and Texas Red PEG_3 azide present on the NDs surface after the click reaction are shown in Figure 25. For an example of fluorescent quenching see Figure 25 (Texas Red, BTTP).

5.4.2 Absorbance

Absorbance measurements were employed to examine CuAAC-click efficiency of three types of ND-PG-alk with different amount of glycidyl propargyl ether used during polymerization. The most efficient click reaction, according to the highest absorbance (the largest relative AUC – area under the curve) was measured for sample ND-PG-alk30 (the biggest amount of glycidyl propargyl ether) (Figure 26). The higher amount of propargyl containing monomer is used for polymerization, the higher is the number of propargyl groups on the surface. Therefore, the concentration of attached sulfonated BODIPY azide was greater. Sample ND-PG-OH was also tested in the click reaction – as a negative control. Measured absorbance is equal to 0, as expected, since there are no alkyne groups present on the surface. ND-PG-alk20 was used in all further optimization experiments.

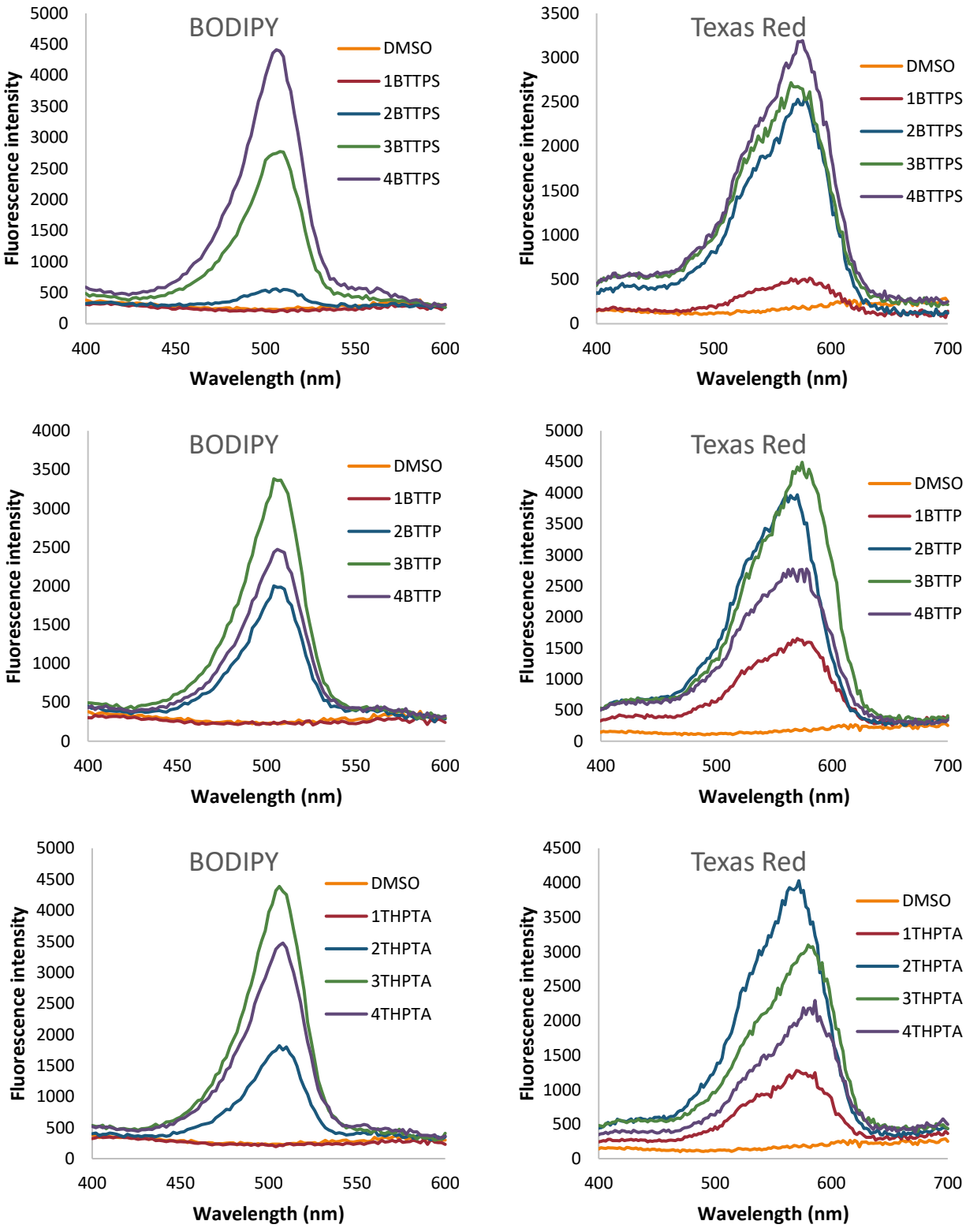

Figure 25 Fluorescence scans reporting CuAAC click reaction efficiency using different conditions; Emission wavelength 510 nm – BODIPY and 580 nm – Texas Red

Next, the effect of various ligands on the click efficiency was investigated with increasing concentration of catalyst. In all these experiments the sample ND-PG-alk20 was used to attach fluorescent dyes, both sulfonated BODIPY azide and Texas Red PEG_3 azide. Absorbance spectra of sulfonated BODIPY azide – ligands comparison at the highest amount of catalyst is shown in (Figure 27), spectra of Texas Red PEG_3 azide (Figure 28). According to the absorbance spectra (Figure 29), we can say, that with the increasing amount of the catalyst (concentration of Cu(II)+ligand mixture) used for the click reaction, the efficiency is growing.

In the case of sulfonated BODIPY attachment on ND-PG-alk20 surface, the most efficient ligand was BTTP followed by THPTA, and BTTPS scored last in respect to experiment. This conclusion was based on the values of AUC obtained from absorbance spectra of BODIPY employing each ligand in the reaction. BTTPS should be, according to the literature, a better ligand that THPTA. However, the decrease in efficiency of CuAAC click reaction of alkyne containing NDs with sulfonated BODIPY azide at the presence of BTTPS, could be influenced by formed electrostatic repulsions because of sulfonyl groups presence. To confirm or disprove our hypothesis we also tried to react the akyne groups on ND with a positively charged Texas Red PEG_3 azide. The results of the click reaction did show BTTPS to be superior to BTTP as we expected. Therefore it can be concluded, that electrostatic repulsion did play a role in the case of sulfonated BODIPY azide.

Lastly, the effect of different concentration of Cu(II) solution was investigated. Four different Cu(II) concentrations were tested. All absorbance results show, that with higher concentration of the catalyst, the reaction efficiency increases.

To sum up, the concentration of the Cu(II) and BTTP solution is the parameter which most influences the reaction efficiency. This result was expected because of known catalytic activity of this complex in the click reaction. BTTP as coordinating ligand was recognized as the most efficient ligand in all the performed reactions. Interesting result is also that the click efficiency increases with the increasing amount of added propargyl containing monomer during synthesis. Therefore, addition of 10 molar % or 20 molar % of glycidyl propargyl ether is not enough for saturation of all reachable –OH groups present in polyglycerol layer.

Based on our results of solvent tests, MeOH seems to be too non-polar for the ND conjugate with clicked BODIPY (polar dye) and too polar for the ND conjugate with Texas Red (non-polar dye). Therefore both click reaction products precipitated from the solution. Dioxane is less polar solvent than all the other used solvents, but NDs with Texas Red also precipitate after the reaction, because in this case, the final conjugate is very poorly soluble in etheric solvents. This was expected and dioxane was used as a negative control. Water was used as the most polar solvent in our experiments, therefore stability of NDs with Texas Red was poor, but NDs with BODIPY were well stable. DMSO belonging to the group of dipolar aprotic solvent can keep in the solution prepared NDs conjugates, both with BODIPY and TexasRed, but slight complexation of Cu(II) can occur during the CuAAC reaction. However, DMSO solubility properties play more important role which can be clearly seen from the reaction efficiency.

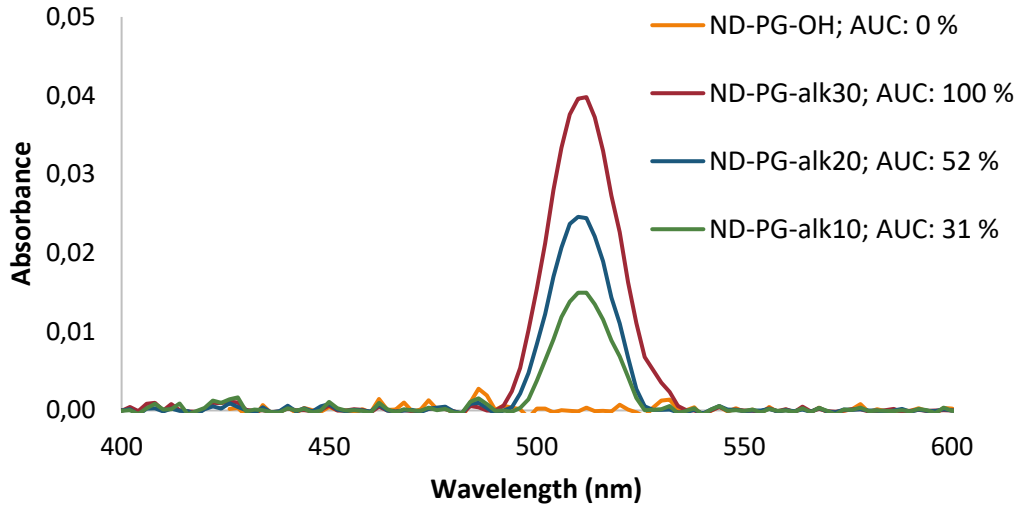

Figure 26 Absorbance spectrum of Sulfonated BODIPY azide reporting CuAAC click reaction efficiency using different monomer ratio during polymerization.

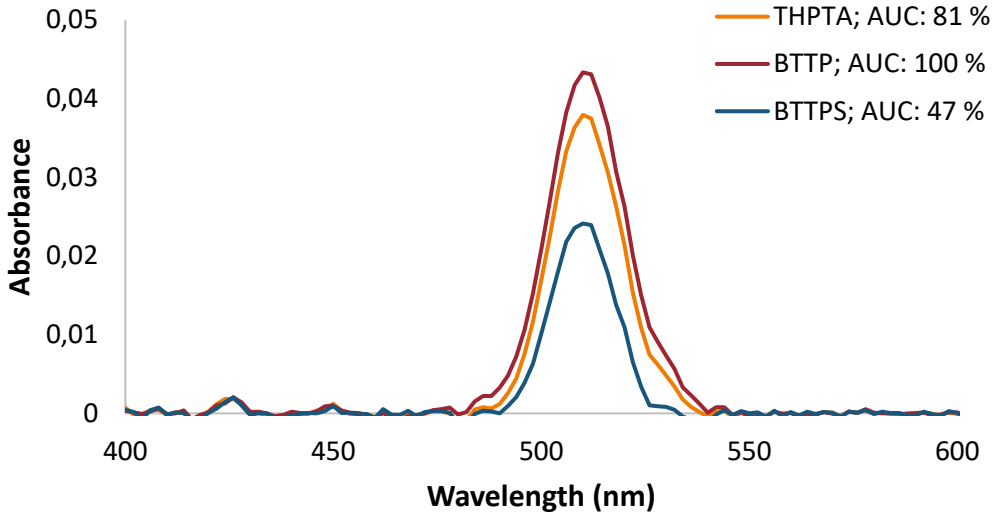

Figure 27 Absorbance spectrum of Sulfonated BODIPY azide reporting CuAAC click reaction efficiency using different conditions

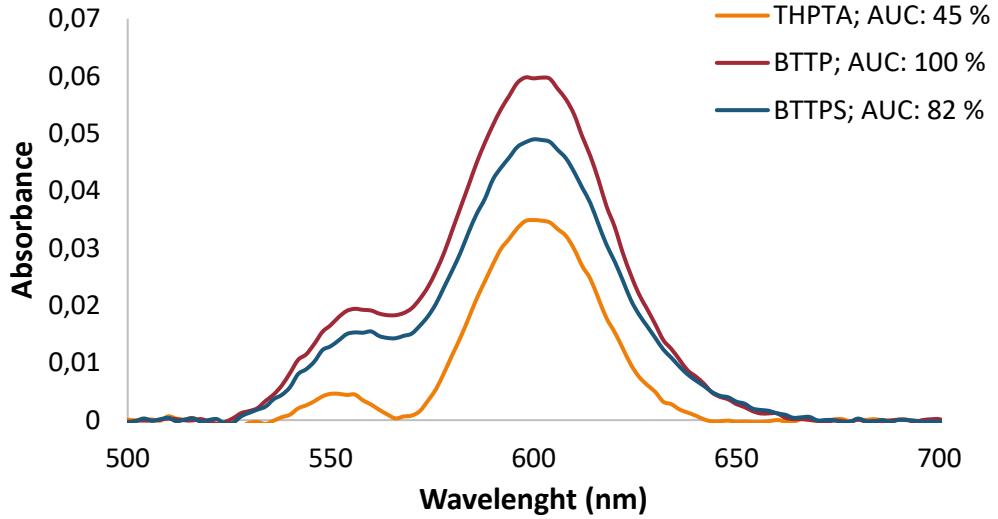

Figure 28 Absorbance spectrum of Texas Red PEG_3 azide reporting CuAAC click reaction efficiency using different conditions

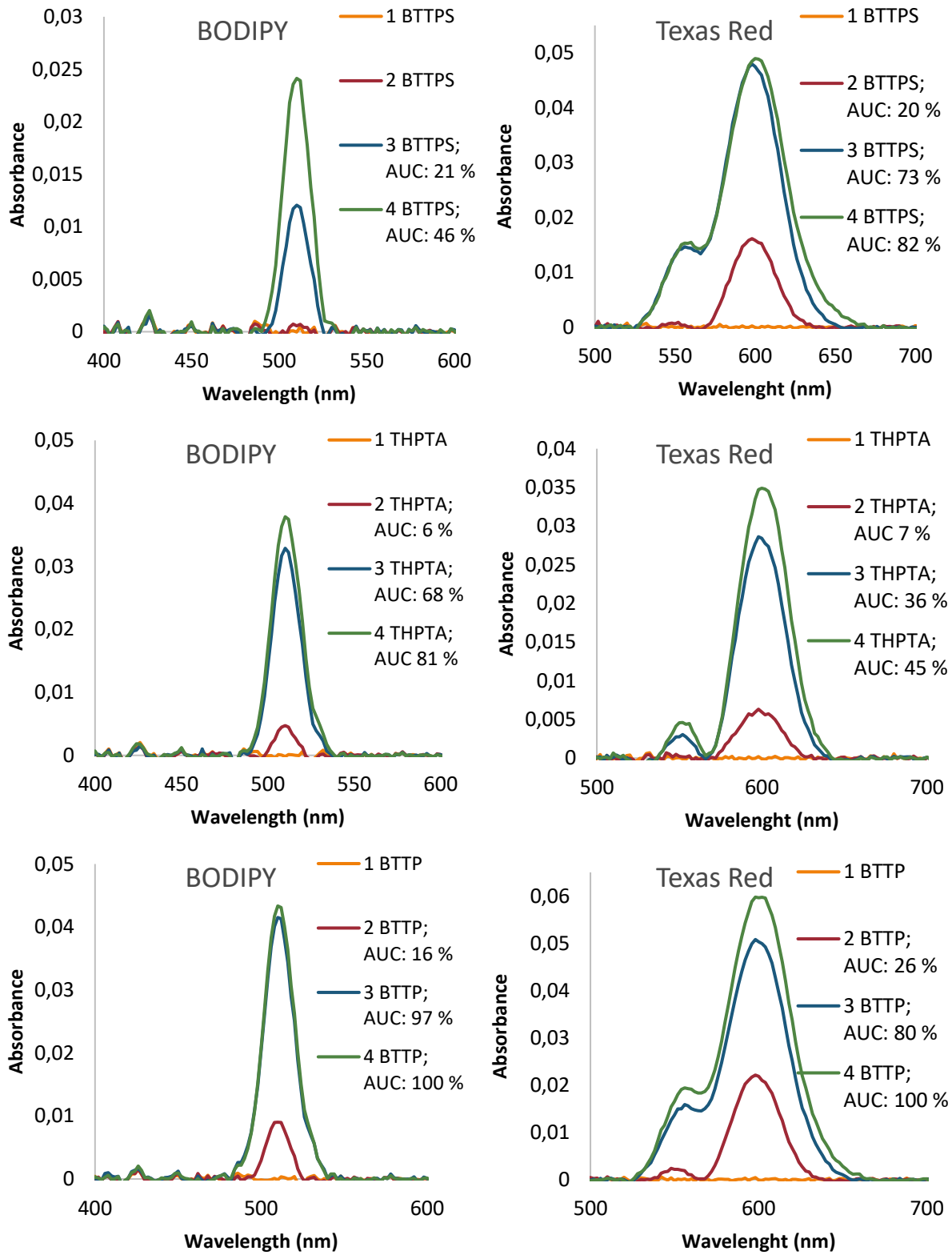

Figure 29 Absorbance spectra of sulfonated BODIPY azide (left) and Texas Red PEG$_3$ azide (right) reporting CuAAC click reaction efficiency using different conditions

5.5 CuAAC click with D-mannose PEG_3 azide

5.5 mg of FND-PG-alk30 were reacted with D-mannose PEG_3 azide, using optimized CuAAC click alkyne-azide cycloaddition conditions, to prepare D-mannosylated FNDs. Optimized conditions are: i) the highest load of glycidyl propargyl ether; ii) the highest Cu(II) (catalyst) concentration; iii) BTTP as ligand. Prepared FND-PG-alk30-man were washed 4x by water. Obtained amount of D-mannosylated NDs was 5.1 mg.

Inertness of these particles towards physiological conditions was further investigated employing stability tests in PBS and FBS media. Results are shown in Chapter 5.6. Presence of attached mannose was examined using FTIR spectroscopy.

5.5.1 FTIR

FTIR spectroscopy was used for characterization of prepared NDs as well as potential direct evidence of mannose attachment to the NDs surface. FTIR spectrum of D-mannosylated NDs (Figure 30) shows several peaks. The most intense transmittance peaks are observed at 1,077 cm^{-1} and 3,045 cm^{-1}, which corresponds to vibration of OH groups from alcohol. Next significant peaks are at 2,918 cm^{-1} and 2,871 cm^{-1}, these were assigned to antisymmetric and symmetric C-H vibrations. The evidence of ester bonds are confirmed by presence signals at 1,727 cm^{-1} and 1,259 cm^{-1}.

FTIR spectra of D-mannosylated NDs were compared with ND and ND-PG samples (Figure 31). All the spectra have intense signal around 3,400 cm^{-1} indicating the presence of (C-O) vibrations corresponding to the alcohol bonds. The obtained FTIR spectra are comparable, and we can see the difference in the relative intensity of D-mannosylated, non-mannosylated ND-PG and NDs without modification. Therefore we could say that D-mannose was successfully attached to prepared fluorescence nanodiamonds.

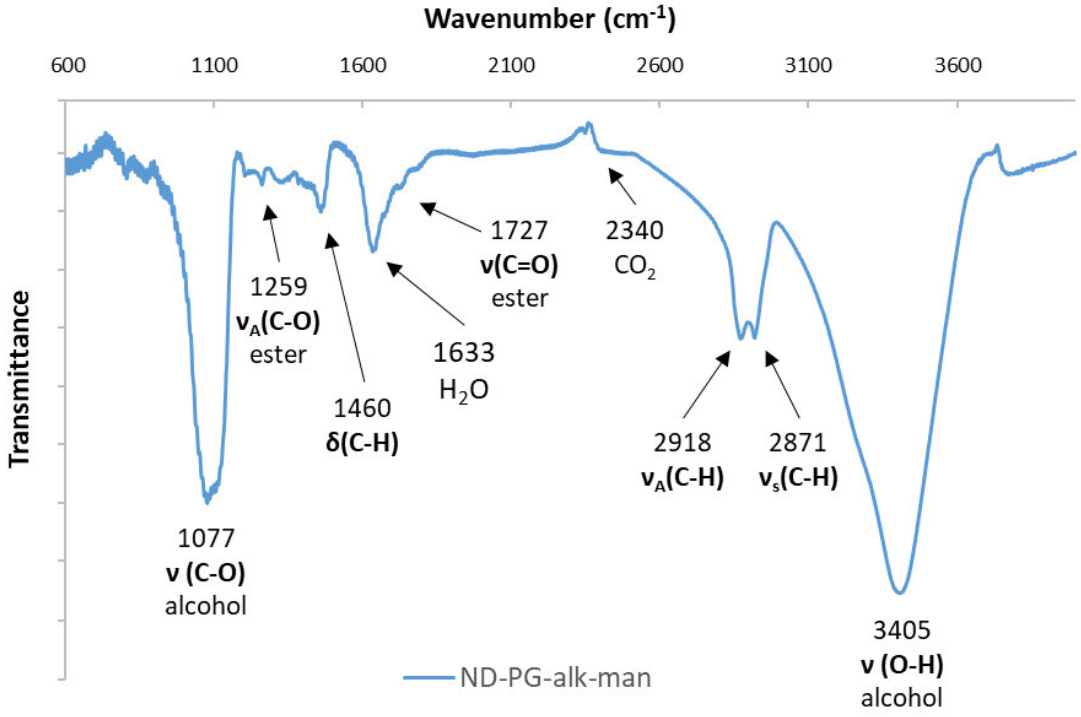

Figure 30 Transmission FTIR spectrum of D-mannosylated ND-PG

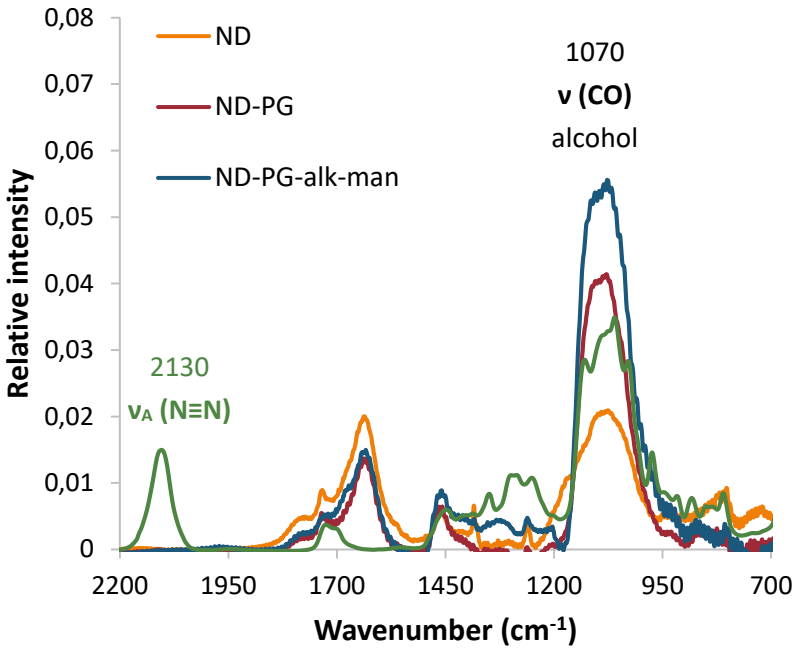

Figure 31 FTIR spectra comparison of ν(CO) signals ND, modified ND

5.6 Stability tests

Stability of prepared NDs was investigated. Media used for these purposes were 1x PBS, 10x PBS and 100 % FBS.

5.6.1 PBS stability test

DLS size measurements of NDs were performed in 1x PBS and 10x PBS at the time 0 h and after 48 h at room temperature. All values corresponding to this test are shown in Table 6. Non-coated NDs are unstable in high-salt concentration and tends to precipitate after their aggregation. Possible up to micron-sized NDs agglomerates formation was examined during the stability test of prepared NDs. This aggregation could be possible because of poor polyglycerol coating, but no large agglomerates of coated NDs were observed.

According to the example autocorrelation data from DLS measurement of ND-PG-alk20 (Figure 32), we can say that also long-term stability in 1x PBS and 10x PBS media is similar to stability in water.

Table 6 DLS results for prepared NDs

Sample	1x PBS 0 h		1x PBS after 48 h		10x PBS 0 h		10x PBS after 48 h	
	d (nm)	PDI	d (nm)	PDI	d (nm)	PDI	d (nm)	PDI
ND-PG-OH	255	0.117	252	0.016	250	0.042	258	0.030
ND-PG-alk10	212	0.089	208	0.078	264	0.146	283	0.099
ND-PG-alk20	207	0.096	193	0.020	260	0.045	260	0.145
ND-PG-alk30	227	0.090	210	0.075	240	0.052	286	0.070
FND-PG-alk30	207	0.191	203	0.050	289	0.036	236	0.185
FND-PG-alk-man30	210	0.051	209	0.045	257	0.008	270	0.136

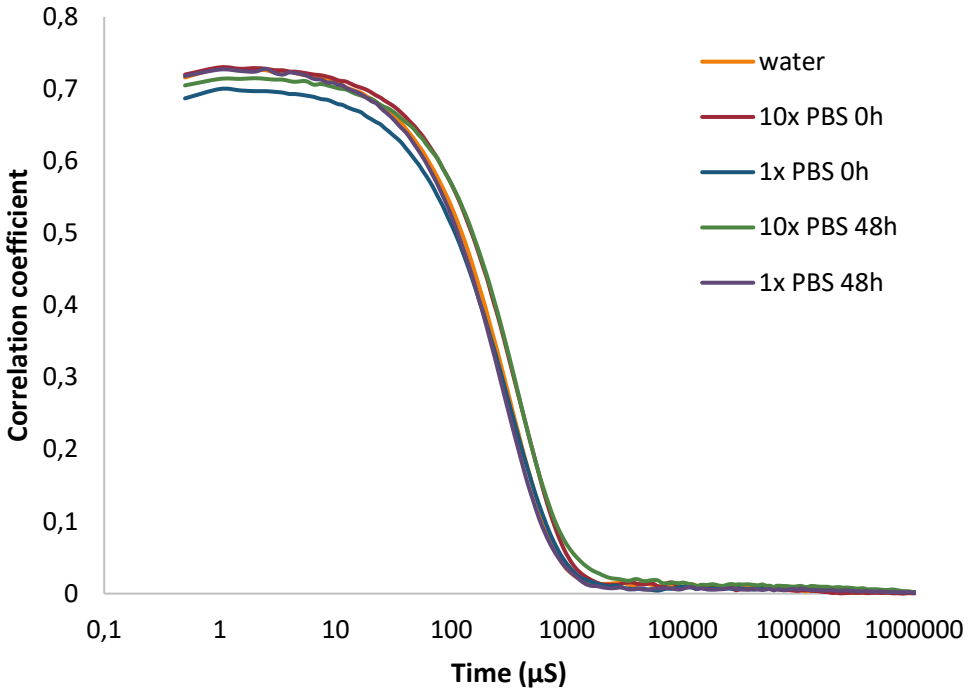

Figure 32 Example of DLS autocorrelation functions for sample FND-PG-alk30

5.6.2 FBS tests

Colloidal stability of prepared PG coated NDs in 100 % FBS medium was investigated. The measurement was performed at 37 °C. 10 subsequent measurements were performed during a period of 30 min. This DLS experiment is appropriate for slow aggregation kinetics study. The mean percentage difference between the NDs sizes was calculated. Values of average hydrodynamic diameter (d ave) with average PDI (PDI ave) and corresponding average percentage difference (Δd ave) are shown in the Table 7. The hydrodynamic diameter of FND-PG-alk30-man is significantly bigger in comparison with the rest values. The differences between size are in the range of instrument error, therefore it can be concluded, that all the particles are extremely stable in FBS medium (Figure 33).

Table 7 DLS results of prepared NDs

	water			FBS 0.5 h		
Sample	**ZP**	**d (nm)**	**PDI**	**d ave (nm)**	**PDI ave**	**Δd ave (%)**
ND-PG-OH	-20	207	0.153	205	0.089	1.80
ND-PG-alk10	-19	211	0.143	210	0.087	2.23
ND-PG-alk20	-22	215	0.080	208	0.096	1.69
ND-PG-alk30	-28	227	0.160	210	0.086	1.53
FND-PG-alk30	-19	217	0.146	214	0.080	1.20
FND-PG-alk-man30	-5	215	0.010	251	0.108	1.49

The values of hydrodynamic diameter of the four ND-PG-alk samples with different alkyne group content, FND-PG-alk30 and D-mannosylated FND-PG-alk were obtained. The measured differences in the NDs size are negligible due to measurement inaccuracy.

Prepared NDs were characterized also by ZP measurement. ZP values of non-mannosylated NDs with a polyglycerol layer is around -20. Negative ZP values may be the consequence of thin PG layer which is not able to shield the negative surface charge of non-reacted carboxylic groups. This observation corresponds with the literature [86]. ZP value of mannosylated FNDs is close to 0. Therefore there is bigger measurement error due to the small charge. However, we are not able to describe the origin of ZP decrease after D-mannosylation of NDs. All ZP values are shown in table Table 7.

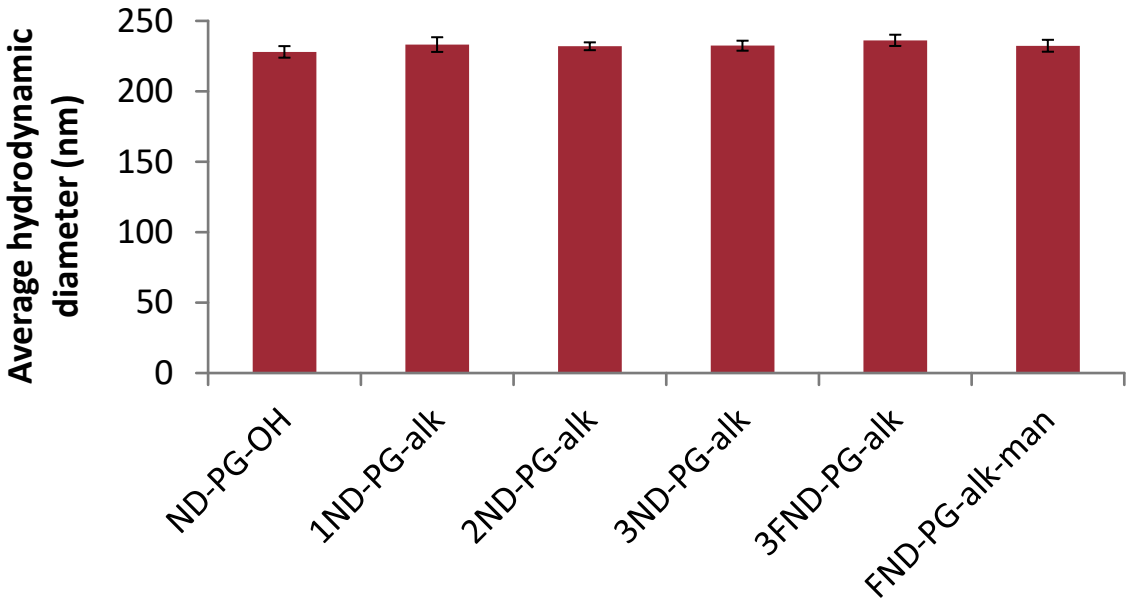

Figure 33 Average hydrodynamic diameter values of various NDs in FBS medium (10 measurements over 30 min); error bars show mean percentage difference

Non-modified NDs are not stable in the environment with high ionic strength and they tend to adsorb biomolecules non-specifically. This kind of non-specific binding is unwanted because it completely hinders the ND's targeting properties. Based on the results obtained during performed stability tests, it can be noticed that prepared polyglycerol-coated NDs are stable in the high-salt concentration media such as PBS. Moreover, non-specific protein binding in FBS was not observed. According to literature, NDs coating with hyperbranched polyglycerol layer significantly suppresses nonspecific adsorption of biomolecules and also self-aggregation [87] and improves long term stability in PBS [41]. However, good stability in our case remains also after propargyl functionalization of polyglycerol layer and further D-mannosylation, which is a quite extraordinary result. We can conclude that our prepared particles are extremely stable, which makes them an ideal candidate for *in vitro* and *in vivo* studies as potential fluorescent imaging probes.

6 CONCLUSION

This thesis was focused on preparation of D-mannosylated fluorescent nanodiamonds coated with a polyglycerol layer for sentinel node(s) visualization.

The theoretical part contains a description of the medical problem, nanodiamonds preparation, their properties, surface chemistry, polymer coating and possible biomedical applications. Methods for NDs characterisation were introduced as well.

The experimental part was focused on the optimisation of glycidol polymerisation on ND's surface and subsequent alkyne group introduction. Based on the results obtained during kinetic studies of glycidol polymerization, the optimum for addition of the second monomer containing alkyne group was found (3 h). The modification was carried out to enable CuAAC click reaction, which was also thoroughly optimised. During the click reaction optimisation, different solvents, various ligands and their concentration were examined. To quantify click efficiency, fluorescent dyes (Sulfonated BODIPY azide and Texas red azide) were used. Not surprisingly, the highest modification by azide dye was obtained using NDs with a higher load of propargyl groups and highest concentration of ligand and Cu(II). BTTP out of three tested ligands was proved to be the most efficient. The optimized conditions were used for D-mannose attachment onto ND's surface (conditions corresponding to maximal click efficiency). Results from thermogravimetry, TEM and DLS show that we are able to coat FNDs with a thin layer of polyglycerol to stabilize them, and we are able to modify NDs with an alkyl group. PG-FNDs are stable in 10x PBS, 1x PBS solutions for 48 h and stability is not affected after D-mannose attachment. The non-specific binding of proteins in FBS media was not observed in both D-mannosylated and non-mannosylated NDs. Presence of mannose was supported by FTIR. Our prepared FNDs, thanks to their promising potential in biomedical applications as sentinel nodes visualisation employing mannose-macrophage targeting, will be further evaluated *in vitro* and *in vivo.*

7 REFERENCES

[1] BRAY, Freddie, Jacques FERLAY, Isabelle SOERJOMATARAM, Rebecca L. SIEGEL, Lindsey A. TORRE and Ahmedin JEMAL. Global cancer statistics 2018: GLOBOCAN estimates of incidence and mortality worldwide for 36 cancers in 185 countries. *CA: A Cancer Journal for Clinicians*. 2018, 68(6), 394-424. DOI: 10.3322/caac.21492. ISSN 00079235.

[2] Morton DL, Wen D, Wong JH, et al. Technical Details of Intraoperative Lymphatic Mapping for Early Stage Melanoma. *Arch Surg*. 1992; 127(4): 392–399. DOI:10.1001/archsurg.1992.01420040034005

[3] Krag DN,Weaver DL, Alex JC, et al. Surgical resection and radiolocalization of the sentinel lymph node in breast cancer using a gamma probe. Surg Oncol 1993;2(6): 335–339; discussion, 340.

[4] Giuliano AE, Kirgan DM, Guenther JM, et al. Lymphatic mapping and sentinel lymphadenectomy for breast cancer. Ann Surg 1994; 220(3): 391–398; discussion, 398–401.

[5] F. ROSES, Daniel and Armando E. GIULIANO. *Breast cancer*. 2nd ed. Philadelphia: Elsevier Churchill Livingstone, 2005, s. 401-459. ISBN 9780443066344.

[6] RANDOLPH, Gwendalyn J., Stoyan IVANOV, Bernd H. ZINSELMEYER and Joshua P. SCALLAN. The Lymphatic System: Integral Roles in Immunity. *Annual Review of Immunology*. 2017, 35(1), 31-52. DOI: 10.1146/annurev-immunol-041015-055354. ISSN 0732-0582.

[7] KUKA, Mirela and Matteo IANNACONE. The role of lymph node sinus macrophages in host defense. *Annals of the New York Academy of Sciences*. 2014, 1319(1), 38-46. DOI: 10.1111/nyas.12387. ISSN 00778923.

[8] BELLOMO, Alicia, Rebecca GENTEK, Marc BAJÉNOFF and Myriam BARATIN. Lymph node macrophages: Scavengers, immune sentinels and trophic effectors. *Cellular Immunology*. 2018, 330, 168-174. DOI: 10.1016/j.cellimm.2018.01.010.

[9] SHIOTA, Takuya, Yuko MIYASATO, Koji OHNISHI, et al. The Clinical Significance of CD169-Positive Lymph Node Macrophage in Patients with Breast Cancer. *PLOS ONE*. 2016, 11(11). DOI: 10.1371/journal.pone.0166680. ISSN 1932-6203.

[10] YUE, Dongfang, Meiling WANG, Fei DENG, Wenting YIN, Haidong ZHAO, Xiaoming ZHAO and Zhaochao XU. Biomarker-targeted fluorescent probes for breast cancer imaging. *Chinese Chemical Letters*. 2018, 29(5), 648-656. DOI: 10.1016/j.cclet.2018.01.046. ISSN 10018417.

[11] EE, Sungsu, Wonbong LIM, Hye-Won RYU, Danbi JO, Jung-Joon MIN, Hyung-Seok KIM and Hoon HYUN. ZW800-1 for Assessment of Blood-Brain Barrier Disruption in and Photothrombotic Stroke Model. *International Journal of Medical Sciences*. 2017, 14(13), 1430-1435. DOI: 10.7150/ijms.22294. ISSN 1449-1907.

[12] QIU, Si-Qi, Guo-Jun ZHANG, Liesbeth JANSEN, Jakob DE VRIES, Carolien P. SCHRÖDER, Elisabeth G.E. DE VRIES and Gooitzen M. VAN DAM. Evolution in sentinel lymph node biopsy in breast cancer. *Critical Reviews in Oncology/Hematology*. 2018, 123, 83-94. DOI: 10.1016/j.critrevonc.2017.09.010. ISSN 10408428.

[13] KEEREWEER, Stijn, Jeroen D. F. KERREBIJN, Pieter B. A. A. VAN DRIEL, et al. Optical Image-guided Surgery—Where Do We Stand?. *Molecular Imaging and Biology*. 2011, 13(2), 199-207. DOI: 10.1007/s11307-010-0373-2. ISSN 1536-1632.

[14] FRANGIONI, J. In vivo near-infrared fluorescence imaging. *Current Opinion in Chemical Biology*. 2003, 7(5), 626-634. DOI: 10.1016/j.cbpa.2003.08.007. ISSN 13675931.

[15] GIOUX, Sylvain, Hak Soo CHOI and John V. FRANGIONI. Image-Guided Surgery Using Invisible Near-Infrared Light: Fundamentals of Clinical Translation. *Molecular Imaging*. 2010, 9(5).

[16] ZHU, Ying, Jing LI, Wenxin LI, et al. The Biocompatibility of Nanodiamonds and Their Application in Drug Delivery Systems. *Theranostics*. 2012, 2(3), 302-312. DOI: 10.7150/thno.3627. ISSN 1838-7640.

[17] VAN DRIEL, P.B.A.A., S. KEEREWEER, T.J.A. SNOEKS and C.W.G.M. LÖWIK. : A Promising Approach for Future Oncologic Surgery. *Comprehensive Biomedical Physics*. Elsevier, 2014, 2014, 301-333. DOI: 10.1016/B978-0-444-53632-7.00422-6. ISBN 9780444536334.

[18] OHNISHI, Shunsuke, Stephen J. LOMNES, Rita G. LAURENCE, Andrew GOGBASHIAN, Giuliano MARIANI and John V. FRANGIONI. Organic Alternatives to Quantum Dots for Intraoperative Near-Infrared Fluorescent Sentinel Lymph Node Mapping. *Molecular Imaging*. 2005, 4(3). DOI: 10.1162/15353500200505127. ISSN 1536-0121.

[19] HENDEROVA, Olga and Nicholas NUNN. Production and purification of nanodiamonds. *Nanodiamonds*. Elsevier, 2017, 2017. 25-56. DOI: 10.1016/B978-0-32-343029-6.00002-7. ISBN 9780323430296.

[20] PALYANOV, Yuri N., Igor N. KUPRIYANOV, Alexander F. KHOKHRYAKOV and Victor G. RALCHENKO. Crystal Growth of Diamond. *Handbook of Crystal Growth*. Elsevier, 2015, 2015, , 671-713. DOI: 10.1016/B978-0-444-63303-3.00017-1. ISBN 9780444633033.

[21] MA, Yanzhang, Guangtian ZOU, Haibin YANG and Jinfang MENG. Conversion of fullerenes to diamond under high pressure and high temperature. *Applied Physics Letters*. 1994, 65(7), 822-823. DOI: 10.1063/1.112242. ISSN 0003-6951.

[22] CAO, Limin, Cunxiao GAO, Haiping SUN and Guangtian ZOU. Synthesis of diamond from carbon nanotubes under high pressure and high temperature. *Carbon*. 2001, 2001(39), 287-324.

[23] DANILENKO, V. V. On the history of the discovery of nanodiamond synthesis. *Physics of the Solid State*. 2004, 46(4), 595-599. DOI: 10.1134/1.1711431. ISSN 1063-7834.

[24] CHANG, C., Y. LIAO, G.Z. WANG, Y.R. MA and R.C. FANG. CVD Diamond Growth. *Crystal Growth Technology*. Elsevier, 2003. 93-141. DOI: 10.1016/B978-081551453-4.50006-3. ISBN 9780815514534.

[25] YANG, G. Laser ablation in liquids. *Progress in Materials Science*. 2007, 52(4), 648-698. DOI: 10.1016/j.pmatsci.2006.10.016. ISSN 00796425.

[26] Stuart. Structure, shape, defects and impurities in nanodiamonds investigated by HRTEM and STEM-EELS. *Nanodiamonds*. Elsevier, 2017, 2017, , 57-84. DOI: 10.1016/B978-0-32-343029-6.00003-9. ISBN 9780323430296.

[27] SAY, J. M., C. BRADAC, C. VAN VREDEN, et al. Fluorescent nanodiamonds for biological applications. *2011 International Quantum Electronics Conference (IQEC) and Conference on Lasers and Electro-Optics (CLEO) Pacific Rim incorporating the Australasian Conference on Optics, Lasers and Spectroscopy and the Australian Conference on Optical Fibre Technology*. IEEE, 2011, 2011,1708-1710. DOI: 10.1109/IQEC-CLEO.2011.6193938. ISBN 978-0-9775657-8-8.

[28] REUSSART, François and Igor I. VLASOV. Photoluminescence of color centers in nanodiamonds. *Nanodiamonds*. Elsevier, 2017, 2017, s. 155-181. DOI: 10.1016/B978-0-32-343029-6.00007-6. ISBN 9780323430296.

[29] CHANG, Be-Ming, Dean HO and Huan-Cheng CHANG. Biomarkers and drug delivery applications. *Nanodiamonds*. Elsevier, 2017, 2017, , 403-417. DOI: 10.1016/B978-0-32-343029-6.00017-9. ISBN 9780323430296.

[30] NEU, Elke. Applications of color centers as nanoscopic sensors. *Nanodiamonds*. Elsevier, 2017, 2017, , 419-438. DOI: 10.1016/B978-0-32-343029-6.00018-0. ISBN 9780323430296.

[31] KRUEGER, Anke. Current issues and challenges in surface chemistry of nanodiamonds. *Nanodiamonds*. Elsevier, 2017, 2017, , 183-242. DOI: 10.1016/B978-0-32-343029-6.00008-8. ISBN 9780323430296.

[32] ZHENG, Wen-Wei, Yi-Han HSIEH, Yu-Chung CHIU, Sian-Jhu CAI, Chia-Liang CHENG and Chinpiao CHEN. Organic functionalization of ultradispersed nanodiamond. *Journal of Materials Chemistry*. 2009, 19(44). DOI: 10.1039/b904302k. ISSN 0959-9428.

[33] MARTÍN, Roberto, Mercedes ÁLVARO, José Raúl HERANCE and Hermenegildo GARCÍA. Fenton-Treated Functionalized Diamond Nanoparticles as Gene Delivery System. *ACS Nano*. 2009, 4(1), 65-74. DOI: 10.1021/nn901616c. ISSN 1936-0851.

[34] OSSWALD, Sebastian, Gleb YUSHIN, Vadym MOCHALIN, Sergei O. KUCHEYEV and Yury GOGOTSI. Control of sp 2 /sp 3 Carbon Ratio and Surface Chemistry of Nanodiamond Powders by Selective Oxidation in Air. *Journal of the American Chemical Society*. 2006, 128(35), 11635-11642. DOI: 10.1021/ja063303n. ISSN 0002-7863.

[35] GORDEEV, S. K. and S. B. KORCHAGINA. On the stability of small-sized nanodiamonds. *Journal of Superhard Materials*. 2007, 29(2), 124-125. DOI: 10.3103/S1063457607020098. ISSN 1063-4576.

[36] RONDIN, L., G. DANTELLE, A. SLABLAB, et al. Surface-induced charge state conversion of nitrogen-vacancy defects in nanodiamonds. *Physical Review B*. 2010, 82(11). DOI: 10.1103/PhysRevB.82.115449. ISSN 1098-0121.

[37] MITEV, D., R. DIMITROVA, M. SPASSOVA, Ch. MINCHEV and S. STAVREV. Surface peculiarities of detonation nanodiamonds in dependence of fabrication and purification methods. *Diamond and Related Materials*. 2007, 16(4-7), 776-780. DOI: 10.1016/j.diamond.2007.01.005. ISSN 09259635.

[38] PICHOT, V., M. COMET, E. FOUSSON, C. BARAS, A. SENGER, F. LE NORMAND and D. SPITZER. An efficient purification method for detonation nanodiamonds. *Diamond and Related Materials*. 2008, 17(1), 13-22. DOI: 10.1016/j.diamond.2007.09.011. ISSN 09259635.

[39] NEBURKOVA, Jitka, Jan VAVRA, Helena RAABOVA, Goutam PRAMANIK, Jan HAVLIK and Petr CIGLER. Nanodiamonds embedded in shells. *Nanodiamonds*. Elsevier, 2017, 2017, , 339-363. DOI: 10.1016/B978-0-32-343029-6.00014-3. ISBN 9780323430296.

[40] BARBEY, Raphael, Laurent LAVANANT, Dusko PARIPOVIC, Nicolas SCHÜWER, Caroline SUGNAUX, Stefano TUGULU and Harm-Anton KLOK. Polymer Brushes via Surface-Initiated Controlled Radical Polymerization: Synthesis, Characterization, Properties, and Applications. *Chemical Reviews*. 2009, 109(11), 5437-5527. DOI: 10.1021/cr900045a. ISSN 0009-2665.

[41] ZHAO, Li, Yong-Hong XU, Tsukasa AKASAKA, Shigeaki ABE, Naoki KOMATSU, Fumio WATARI and Xiao CHEN. Polyglycerol-coated nanodiamond as a macrophage-evading platform for selective drug delivery in cancer cells. *Biomaterials*. 2014, 35(20), 5393-5406. DOI: 10.1016/j.biomaterials.2014.03.041. ISSN 01429612.

[42] LHADDAD, Anna, Catherine DURIEU, Géraldine DANTELLE, Eric LE CAM, Claude MALVY, François TREUSSART, Jean-Rémi BERTRAND and Heidar-Ali TAJMIR-RIAHI. Influence of the Internalization Pathway on the Efficacy of siRNA Delivery by Cationic Fluorescent Nanodiamonds in the Ewing Sarcoma Cell Model. *PLoS ONE*. 2012, 7(12). DOI: 10.1371/journal.pone.0052207. ISSN 1932-6203.

[43] ZHAO, Li, Yuki NAKAE, Hongmei QIN, Tadamasa ITO, Takahide KIMURA, Hideto KOJIMA, Lawrence CHAN and Naoki KOMATSU. Polyglycerol-functionalized nanodiamond as a platform for gene delivery: Derivatization, characterization, and hybridization with DNA. *Beilstein Journal of Organic Chemistry*. 2014, 10, 707-713. DOI: 10.3762/bjoc.10.64. ISSN 1860-5397.

[44] J NEBURKOVA, Jitka, Jan VAVRA and Petr CIGLER. Coating nanodiamonds with biocompatible shells for applications in biology and medicine. *Current Opinion in Solid State and Materials Science*. 2017, 21(1), 43-53. DOI: 10.1016/j.cossms.2016.05.008. ISSN 13590286.

[45] WANG, Dongxin, Yingqi LI, Zhimei TIAN, Ruixia CAO and Binsheng YANG. Transferrin-conjugated nanodiamond as an intracellular transporter of chemotherapeutic drug and targeting therapy for cancer cells. *Therapeutic Delivery*. 2014, 5(5), 511-524. DOI: 10.4155/tde.14.17. ISSN 2041-5990.

[46] ZHANG, Bailin, Yingqi LI, Chia-Yi FANG, Cheng-Chun CHANG, Chao-Sheng CHEN, Yi-Ying CHEN and Huan-Cheng CHANG. Receptor-Mediated Cellular Uptake of Folate-Conjugated Fluorescent Nanodiamonds: A Combined Ensemble and Single-Particle Study. *Small*. 2009, 5(23), 2716-2721. DOI: 10.1002/smll.200900725. ISSN 16136810.

[47] DONG, Yu, Ruixia CAO, Yingqi LI, Zhiqin WANG, Lin LI and Lu TIAN. Folate-conjugated nanodiamond for tumor-targeted drug delivery. *RSC Advances*. 2015, 5(101), 82711-82716. DOI: 10.1039/C5RA12383F. ISSN 2046-2069.

[48] MARCON, Lionel, Zoulika KHERROUCHE, Joël LYSKAWA, David FOURNIER, David TULASNE, Patrice WOISEL and Rabah BOUKHERROUB. Preparation and characterization of Zonyl-coated nanodiamonds with antifouling properties. *Chemical Communications*. 2011, 47(18). DOI: 10.1039/c1cc10338e. ISSN 1359-7345.

[49] ZHAO, Li, Yong-Hong XU, Hongmei QIN, et al. Platinum on Nanodiamond: A Promising Prodrug Conjugated with Stealth Polyglycerol, Targeting Peptide and Acid-Responsive Antitumor Drug. *Advanced Functional Materials*. 2014, 24(34), 5348-5357. DOI: 10.1002/adfm.201304298. ISSN 1616301X.

[50] SLEGEROVA, Jitka, Miroslav HAJEK, Ivan REHOR, Frantisek SEDLAK, Jan STURSA, Martin HRUBY and Petr CIGLER. Designing the nanobiointerface of fluorescent nanodiamonds: highly selective targeting of glioma cancer cells. *Nanoscale*. 2015, 7(2), 415-420. DOI: 10.1039/C4NR02776K. ISSN 2040-3364.

[51] CHEN, Junyu, Meiying LIU, Qiang HUANG, et al. A novel light-induced ATRP for the preparation of water dispersible fluorescent nanodiamonds and their biological imaging applications. *Ceramics International*. 2018, 44(8), 9907-9914. DOI: 10.1016/j.ceramint.2018.03.011. ISSN 02728842.

[52] SHI, Yingge, Meiying LIU, Ke WANG, et al. Direct surface PEGylation of nanodiamond via RAFT polymerization. *Applied Surface Science*. 2015, 357, 2147-2153. DOI: 10.1016/j.apsusc.2015.09.200. ISSN 01694332.

[53] SHARPLESS, K.B., M.G. FINN and H.C. KOLB. Click Chemistry: Diverse Chemical Function from a Few Good Reactions. *Angewandte Chemie International Edition*. 2001, 2001(Vol 40, 11), 2004-2021.

[54] Kolb, H.C., Sharpless, B.K., 2003. The growing impact of click chemistry on drug discovery. Drug Discov. Today 8, 1128–1137.

[55] MAKISHIMA, Akio. Click Chemistry-Related Topics. *Biochemistry for Materials Science*. Elsevier, 2019, , 239-245. DOI: 10.1016/B978-0-12-817054-0.00021-7. ISBN 9780128170540.

[56] HONG, Vu, Stanislav I. PRESOLSKI, Celia MA and M. G. FINN. Analysis and Optimization of Copper-Catalyzed Azide-Alkyne Cycloaddition for Bioconjugation. *Angewandte Chemie International Edition*. 2009, 48(52), 9879-9883. DOI: 10.1002/anie.200905087. ISSN 14337851.

[57] JIN, Liqun, Daniel R. TOLENTINO, Mohand MELAIMI and Guy BERTRAND. Isolation of bis(copper) key intermediates in Cu-catalyzed azide-alkyne "click reaction". *Science Advances*. 2015, 1(5). DOI: 10.1126/sciadv.1500304. ISSN 2375-2548.

[58] PRESOLSKI, Stanislav I., Vu Phong HONG and M.G. FINN. Copper-Catalyzed Azide-Alkyne Click Chemistry for Bioconjugation. *Current Protocols in Chemical Biology*. Hoboken, NJ, USA, 2009, 2011. DOI: 10.1002/9780470559277.ch110148. ISBN 9780470559277.

[59] WANG, Wei, Senglian HONG, Andrew TRAN, Hao JIANG, Rebecca TRIANO, Yi LIU, Xing CHEN and Peng WU. Sulfated Ligands for the Copper(I)-Catalyzed Azide-Alkyne Cycloaddition. Chemistry - An Asian Journal. 2011, 6(10), 2796-2802. DOI: 10.1002/asia.201100385. ISSN 18614728.

[60] HUYNH, Vien T., Samuel PEARSON, Janina-Miriam NOY, Amanda ABBOUD, Robert H. UTAMA, Hongxu LU and Martina H. STENZEL. Nanodiamonds with Surface Grafted Polymer Chains as Vehicles for Cell Imaging and Cisplatin Delivery: Enhancement of Cell Toxicity by POEGMEMA Coating. *ACS Macro Letters*. 2013, 2(3), 246-250. DOI: 10.1021/mz4000199. ISSN 2161-1653.

[61] MOHAN, Nitin, Chao-Sheng CHEN, Hsiao-Han HSIEH, Yi-Chun WU and Huan-Cheng CHANG. In Vivo Imaging and Toxicity Assessments of Fluorescent Nanodiamonds in Caenorhabditis elegans. *Nano Letters*. 2010, 10(9), 3692-3699. DOI: 10.1021/nl1021909. ISSN 1530-6984.

[62] VAIJAYANTHIMALA, V., Po-Yun CHENG, Shih-Hua YEH, Kuang-Kai LIU, Cheng-Hsiang HSIAO, Jui-I CHAO and Huan-Cheng CHANG. The long-term stability and biocompatibility of fluorescent nanodiamond as an in vivo contrast agent. *Biomaterials*. 2012, 33(31), 7794-7802. DOI: 10.1016/j.biomaterials.2012.06.084. ISSN 01429612.

[63] CHANG, Be-Ming, Hsin-Hung LIN, Long-Jyun SU, et al. Highly Fluorescent Nanodiamonds Protein-Functionalized for Cell Labeling and Targeting. *Advanced Functional Materials*. 2013, 23(46), 5737-5745. DOI: 10.1002/adfm.201301075. ISSN 1616301X.

[64] LIN, Hsin-Hung, Hsiao-Wen LEE, Ruey-Jen LIN, et al. Tracking and Finding Slow-Proliferating/Quiescent Cancer Stem Cells with Fluorescent Nanodiamonds. *Small*. 2015, 11(34), 4394-4402. DOI: 10.1002/smll.201500878. ISSN 16136810.

[65] HSU, Tzu-Chia, Kuang-Kai LIU, Huan-Cheng CHANG, Eric HWANG and Jui-I CHAO. Labeling of neuronal differentiation and neuron cells with biocompatible fluorescent nanodiamonds. *Scientific Reports*. 2015, 4(1). DOI: 10.1038/srep05004. ISSN 2045-2322.

[66] CHIPAUX, Mayeul, Kiran J. VAN DER LAAN, Simon R. HEMELAAR, Masoumeh HASANI, Tingting ZHENG and Romana SCHIRHAGL. Nanodiamonds and Their Applications in Cells. *Small*. 2018, 14(24) . DOI: 10.1002/smll.201704263. ISSN 16136810.

[67] FAKLARIS, Orestis, Damien GARROT, Vandana JOSHI, et al. Detection of Single Photoluminescent Diamond Nanoparticles in Cells and Study of the Internalization Pathway. *Small*. 2008, 4(12), 2236-2239. DOI: 10.1002/smll.200800655. ISSN 16136810.

[68] CHANG, Xue-Qing, Mark CHEN, Robert LAM, Xiaoyang XU, Eiji OSAWA and Dean HO. Polymer-Functionalized Nanodiamond Platforms as Vehicles for Gene Delivery. *ACS Nano*. 2009, 3(9), 2609-2616. DOI: 10.1021/nn900865g. ISSN 1936-0851.

[69] DANIELS, Tracy R., Tracie DELGADO, Jose A. RODRIGUEZ, Gustavo HELGUERA and Manuel L. PENICHET. The transferrin receptor part I: Biology and targeting with cytotoxic antibodies for the treatment of cancer. *Clinical Immunology*. 2006, 121(2), 144-158. DOI: 10.1016/j.clim.2006.06.010. ISSN 15216616.

[70] PETRÁKOVÁ, Vladimíra, Miloš NESLÁDEK, Andrew TAYLOR, et al. Luminescence properties of engineered nitrogen vacancy centers in a close surface proximity. *Physica status solidi (a)*. 2011, 208(9), 2051-2056. DOI: 10.1002/pssa.201100035. ISSN 18626300.

[71] PETRAKOVA, V., I. REHOR, J. STURSA, M. LEDVINA, M. NESLADEK and P. CIGLER. Charge-sensitive fluorescent nanosensors created from nanodiamonds. *Nanoscale*. 2015, 7(29), 12307-12311. DOI: 10.1039/C5NR00712G. ISSN 2040-3364.

[72] KRANZ, Christine and Boris MIZAIKOFF. Nanomaterials: Characterization Methods. *Reference Module in Chemistry, Molecular Sciences and Chemical Engineering*. Elsevier, 2018, 2018. DOI: 10.1016/B978-0-12-409547-2.13994-0. ISBN 9780124095

[73] BARHOUM, Ahmed and M. LUISA GARCÍA-BETANCOURT. Physicochemical characterization of nanomaterials: size, morphology, optical, magnetic, and electrical properties. *Emerging Applications of Nanoparticles and Architecture Nanostructures*. Elsevier, 2018, 2018, 279-304. DOI: 10.1016/B978-0-323-51254-1.00010-5. ISBN 9780323512541.

[74] GÓMEZ-MERINO, A.I., F.J. RUBIO-HERNÁNDEZ, J.F. VELÁZQUEZ-NAVARRO, J. AGUIAR and C. JIMÉNEZ-AGREDANO. Study of the aggregation state of anatase water nanofluids using rheological and DLS methods. *Ceramics International*. 2014, 40(9), 14045-14050. DOI: 10.1016/j.ceramint.2014.05.132. ISSN 02728842.

[75] BRAR, Satinder K. and M. VERMA. Measurement of nanoparticles by light-scattering techniques. *TrAC Trends in Analytical Chemistry*. 2011, 30(1), 4-17. DOI: 10.1016/j.trac.2010.08.008. ISSN 01659936.

[76] GLATTER, Otto. Dynamic Light Scattering (DLS). *Scattering Methods and their Application in Colloid and Interface Science*. Elsevier, 2018,223-263. DOI: 10.1016/B978-0-12-813580-8.00011-0. ISBN 9780128135808.

[77] BHATTACHARJEE, Sourav. DLS and zeta potential – What they are and what they are not?. *Journal of Controlled Release*. 2016, 235, 337-351. DOI: 10.1016/j.jconrel.2016.06.017. ISSN 01683659.

[78] TITUS, Deena, E. JAMES JEBASEELAN SAMUEL and Selvaraj Mohana ROOPAN. Nanoparticle characterization techniques. *Green Synthesis, Characterization and Applications of Nanoparticles*. Elsevier, 2019, 303-319. DOI: 10.1016/B978-0-08-102579-6.00012-5. ISBN 9780081025796.

[79] XU, Renliang. Progress in nanoparticles characterization: Sizing and zeta potential measurement. *Particuology*. 2008, 6(2), 112-115. DOI: 10.1016/j.partic.2007.12.002. ISSN 16742001.

[80] TANG, C.Y. and Z. YANG. Transmission Electron Microscopy (TEM). *Membrane Characterization*. Elsevier, 2017, 145-159. DOI: 10.1016/B978-0-444-63776-5.00008-5. ISBN 9780444637765.

[81] PÉREZ-ARANTEGUI, Josefina. Electron Microscopy. *Reference Module in Chemistry, Molecular Sciences and Chemical Engineering*. Elsevier, 2017. DOI: 10.1016/B978-0-12-409547-2.14228-3. ISBN 9780124095472.

[82] WANG, K., B. CAO, J. CHEN and W. ZHOU. TEM studies of nanostructures. *Modelling, Characterization, and Production of Nanomaterials*. Elsevier, 2015, 115-144. DOI: 10.1016/B978-1-78242-228-0.00004-1. ISBN 9781782422280.

[83] CAKMAK, Onur, Caglar ELBUKEN, Erhan ERMEK, Aref MOSTAFAZADEH, Ibrahim BARIS, B. ERDEM ALACA, Ibrahim Halil KAVAKLI and Hakan UREY. Microcantilever based disposable viscosity sensor for serum and blood plasma measurements. *Methods*. 2013, 63(3), 225-232. DOI: 10.1016/j.ymeth.2013.07.009. ISSN 10462023.

[84] REHOR, Ivan and Petr CIGLER. Precise estimation of HPHT nanodiamond size distribution based on transmission electron microscopy image analysis. *Diamond and Related Materials*. 2014, 46, 21-24. DOI: 10.1016/j.diamond.2014.04.002. ISSN 09259635.

[85] HOLGATE, J.H. and J. WEBB. MICROSCOPY Transmission Electron Microscopy. *Encyclopedia of Food Sciences and Nutrition*. Elsevier, 2003 s. 3928-3934. DOI: 10.1016/B0-12-227055-X/00780-X. ISBN 9780122270550.

[86] ZHAO, Li, Yuki NAKAE, Hongmei QIN, Tadamasa ITO, Takahide KIMURA, Hideto KOJIMA, Lawrence CHAN and Naoki KOMATSU. Polyglycerol-functionalized nanodiamond as a platform for gene delivery: Derivatization, characterization, and hybridization with DNA. *Beilstein Journal of Organic Chemistry*. 2014, 10, 707-713. DOI: 10.3762/bjoc.10.64. ISSN 1860-5397.

[87] ZHAO, Li, Akihiko SHIINO, Hongmei QIN, Takahide KIMURA and Naoki KOMATSU. Synthesis, Characterization, and Magnetic Resonance Evaluation of Polyglycerol-Functionalized Detonation Nanodiamond Conjugated with Gadolinium(III) Complex. *Journal of Nanoscience and Nanotechnology*. 2015, 15(2), 1076-1082. DOI: 10.1166/jnn.2015.9738. ISSN 15334880.

8 ABBREVIATIONS

AIBN	Azobisisobutyronitrile
ALS	Asymmetric least square
ATRP	Atom transfer radical polymerization
BSA	Bovine serum albumin
BTTP	3-[4-({bis[(1-tert-butyl-1H-1,2,3-triazol-4-yl)methyl]amino} methyl)-1H-1,2,3-triazol-1-yl]propanol
BTTPS	3-[4-({bis[(1-tert-butyl-1H-1,2,3-triazol-4-yl)methyl]amino} methyl)-1H-1,2,3-triazol-1-yl]propyl hydrogen sulfate
CCD	Charge-coupled detectors
CD206	Mannose receptor
CD209b	SIGN-R1 receptor
CDCs	Cancer stem cells
CTA	Chain transfer agent
CuAAC	Copper(I)-catalyzed azide-alkyne cycloaddition
CVD	Chemical vapour deposition
DLS	Dynamic light scattering
DMSO	Dimethylsulfoxide
DND	Detonation nanodiamond
DNDs	Detonation nanodiamonds
EB	Evans blue
EDL	Adsorbed double layer
FBS	Fetal bovine serum
FDA	Food and Drug Administration
FLIM	Fluorescence lifetime imaging microscopy
FND-PG-alk30	Alkyne terminated polyglycerol coated nanodiamonds (molar ratio of glycidol:glycidyl propargyl ether is equal to 70:30)
FND-PG-alk30-man	D-mannosylated fluorescent nanodiamonds
FNDs	Fluorescent nanodiamonds
FTIR	Fourier-transform infrared spectroscopy
HEPES	4-(2-hydroxyethyl)-1-piperazineethanesulfonic acid
HPHT	High-pressure high-temperature
HR-TEM	High-resolution transmission electron microscopy
HSA	Human serum albumin
ICG	Indocyanine green
LCs	Lung stem cells
MB	Methylene blue
MSM	Medullary sinus macrophages
ND	Nanodiamond
ND-PG-alk	Alkyne terminated polyglycerol coated nanodiamonds
ND-PG-alk10	Alkyne terminated polyglycerol coated nanodiamonds (molar ratio of glycidol:glycidyl propargyl ether is equal to 90:10)
ND-PG-alk20	Alkyne terminated polyglycerol coated nanodiamonds (molar ratio of glycidol:glycidyl propargyl ether is equal to 80:20)
ND-PG-alk30	Alkyne terminated polyglycerol coated nanodiamonds (molar ratio of glycidol:glycidyl propargyl ether is equal to 70:30)

ND-PG-OH	Polyglycerol coated nanodiamonds
NDs	Nanodiamonds
NIR	Near Infrared
NPs	Nanoparticles
NV^-	Negatively charged nitrogen-vaccancy centre
PAH	Poly(allylamine hydrochloride)
PBS	Phosphate buffer saline
PBV	Isosulfan blue or patent blue V
PDMAEMA	Poly[2- dimethylamino)ethyl methacrylate]
PEG	Poly(ethylene glycol)
PEI	Poly(ethylene-imine)
PG	Poly(glycerol)
PHPMA	Poly[N-(2-hydroxypropyl) methacrylamide]
PNIPAM	Poly(N-isopropylacrylamide)
PPEGMA	Poly(PEG methyl ether methacrylate)
RAFT	Reversible addition-fragmentation chain transfer
RGD	Tripeptide Arg-Gly-Asp
SLN	Sentinel lymph node
SSM	Subcapsular sinus macrophages
STEM	Scanning transmission electron microscopy
TBR	Tumour to background ratio
TEM	Transmission electron microscopy
TGA	Thermogravimetric analysis
THPTA	Tris-hydroxypropyltriazolylmethylamine
ZP	Zeta potential